CrossMark

Studying Magnetic Fields and Dust in M17 Using Polarized Thermal Dust Emission Observed by SOFIA/HAWC+

Thuong Duc Hoang[1,2] , Nguyen Bich Ngoc[3,4] , Pham Ngoc Diep[3] , Le Ngoc Tram[5,6] , Thiem Hoang[7,8] , Kate Pattle[9] ,
Wanggi Lim[5] , Ngan Le[10], Dieu D. Nguyen[11,12] , Nguyen Thi Phuong[3,7], Nguyen Fuda[11,12] , Tuan Van Bui[2],
Gia Bao Truong Le[11,12] , Hien Phan[2] , and Nguyen Chau Giang[7]

[1] Kavli Institute for the Physics and Mathematics of the Universe (Kavli IPMU, WPI), UTIAS, The University of Tokyo, Kashiwa, Chiba 277-8583, Japan
hoang-duc.thuong@usth.edu.vn
[2] University of Science and Technology of Hanoi (USTH), Vietnam Academy of Science and Technology (VAST), 18 Hoang Quoc Viet, Hanoi, Vietnam
[3] Department of Astrophysics, Vietnam National Space Center, Vietnam Academy of Science and Technology, 18 Hoang Quoc Viet, Hanoi, Vietnam
[4] Graduate University of Science and Technology, Vietnam Academy of Science and Technology, 18 Hoang Quoc Viet, Hanoi, Vietnam
[5] Stratospheric Observatory for Infrared Astronomy, Universities Space Research Association, NASA Ames Research Center, MS 232-11, Moffett Field, 94035
CA, USA
[6] Max-Planck-Institut für Radioastronomie, Auf dem Hügel 69, D-53-121, Bonn, Germany
[7] Korea Astronomy and Space Science Institute, 776 Daedeokdae-ro, Yuseong-gu, Daejeon 34055, Republic of Korea
[8] University of Science and Technology, Korea, 217 Gajeong-ro, Yuseong-gu, Daejeon 34113, Republic of Korea
[9] Department of Physics and Astronomy, University College London, Gower Street, London WC1E 6BT, UK
[10] Institute of Astronomy, Faculty of Physics, Astronomy and Informatics, Nicolaus Copernicus University, Grudziadzka 5, 87-100 Torun, Poland
[11] Department of Physics, International University, Quarter 6, Linh Trung Ward, Thu Duc City, Ho Chi Minh City, Vietnam
[12] Vietnam National University, Ho Chi Minh City, Vietnam

Abstract

We report on the highest spatial resolution measurement to date of magnetic fields (B-fields) in M17 using thermal dust polarization measurements taken by SOFIA/HAWC+ centered at a wavelength of 154 μm. Using the Davis–Chandrasekhar–Fermi method, in which the polarization angle dispersion calculated using the structure function technique is the quantity directly observed by SOFIA/HAWC+, we found the presence of strong B-fields of 980 ± 230 and 1665 ± 885 μG in the lower-density M17-N and higher-density M17-S regions, respectively. The B-field morphology in M17-N possibly mimics the fields in gravitationally collapsing molecular cores, while in M17-S the fields run perpendicular to the density structure. M17-S also displays a pillar feature and an asymmetric large-scale hourglass-shaped field. We use the mean B-field strengths to determine Alfvénic Mach numbers for both regions, finding that B-fields dominate over turbulence. We calculate the mass-to-flux ratio, λ, finding $\lambda = 0.07$ for M17-N and 0.28 for M17-S. These subcritical λ values are consistent with the lack of massive stars formed in M17. To study dust physics, we analyze the relationship between dust polarization fraction, p, emission intensity, I, gas column density, $N(H_2)$, polarization angle dispersion function, S, and dust temperature, T_d. p decreases with intensity as $I^{-\alpha}$ with $\alpha = 0.51$. p tends to first increase with T_d, but then decreases at higher T_d. The latter feature, seen in M17-N at high T_d when $N(H_2)$ and S decrease, is evidence of the radiative torque disruption effect.

Unified Astronomy Thesaurus concepts: Interstellar magnetic fields (845); Astrophysical magnetism (102); Magnetic fields (994); Star forming regions (1565); Stellar winds (1636); Star formation (1569); Interstellar dust (836); Interstellar dust processes (838)

1. Introduction

Star formation is a complex process that involves self-gravity, turbulence, magnetic fields, and stellar feedback. Understanding the exact role of magnetic fields in the evolution of molecular clouds (MCs) and in the star formation process is a challenge of modern astrophysics. In the past decades, evidence has emerged to suggest the importance of magnetic fields (B-fields) in the evolution of MCs and star formation (McKee & Ostriker 2007; Ward-Thompson et al. 2020). There are two types of B-field models, in which B-fields play contrasting roles. First, strong B-field models support a paradigm in which magnetic pressure acts against the gravitational collapse of MCs. This magnetic support is lost when the ratio of the core mass to the magnetic flux exceeds a

critical value, beyond which the cloud enters into a state of gravitational collapse to form a new star (Nakano & Nakamura 1978). Second, in the weak-field models, B-fields are sufficiently weak that the dynamics of MCs are dominated by turbulence. Star formation takes place in filaments that are likely produced at the intersection of supersonic turbulent flows (e.g., Padoan & Nordlund 1999; Elmegreen 2000; Mac Low & Klessen 2004; Crutcher 2012). It is thus necessary to observe B-fields in specific MCs (e.g., M17 in this work) to investigate their effects on star formation and on the subsequent evolution of the entire cloud, in order to test these theoretical predictions (Seifried & Walch 2015; Federrath 2016; Li & Klein 2019; Ward-Thompson et al. 2020).

Dust polarization arising from aligned dust grains is widely used to map B-fields (see, e.g., Crutcher 2012). This relies on thermal dust emission being preferentially polarized perpendicular to the local B-field direction. This assumption is valid in most astrophysical environments (e.g., the diffuse interstellar medium (ISM) and MCs) where grain alignment occurs with the shortest axis parallel to the magnetic field (see

Hoang et al. 2021). However, in very dense regions such as protostellar cores and disks, grain alignment may occur with their shortest axis perpendicular to the B-fields, due to inefficient internal relaxation (Hoang & Lazarian 2009; Hoang et al. 2021). In particular, in intense radiation fields, radiative torques can cause grains to align with their shortest axis along the radiation field direction instead of along the magnetic field (Lazarian & Hoang 2007). The strength of these B-fields can then be estimated using the Davis–Chandrasekhar–Fermi (DCF) method (Davis 1951; Chandrasekhar & Fermi 1953). The DCF method indirectly measures B-field strength from the B-field fluctuations that are encoded in the observed dispersion in dust polarization direction. Although Planck has provided a full-sky map of dust polarization at 353 GHz (see, e.g., Planck Collaboration et al. 2015), and many studies of B-fields at MC scales have been performed, including of filament structures and star-forming cores (see, e.g., Dotson 1996; Houde et al. 2002; Pellegrini et al. 2007; Chen et al. 2012; Pattle et al. 2017, 2018; Wurster & Li 2018; Chuss et al. 2019; Hennebelle & Inutsuka 2019; Sugitani et al. 2019), dust polarization data at higher resolutions are still lacking. Recently, the Atacama Large Millimeter/submillimeter Array has started to provide high-resolution polarization observations (e.g., Beuther et al. 2020; Liu et al. 2020; Sanhueza et al. 2021).

Dust polarization also allows us to gain insight into fundamental properties of dust grains such as grain shapes, size distribution, and alignment. Grain alignment is a long-standing problem in astrophysics. The leading theory of grain alignment is the RAdiative Torque Alignment theory (RAT-A; Draine & Weingartner 1997; Lazarian & Hoang 2007; Hoang & Lazarian 2016) (see, e.g., Andersson et al. 2015; Lazarian et al. 2015, for reviews). RAdiative Torques (RATs) arising from the interaction of an anisotropic radiation field with an irregular grain were first suggested by Dolginov & Mytrophanov (1976), and later numerically demonstrated by Draine & Weingartner (1996), and analytically modeled by Lazarian & Hoang (2007). The grain alignment efficiency due to RAT-A is found to increase with increasing radiation field or dust temperature (see Hoang et al. 2021), which results in an increase of the polarization fraction with dust temperature (Lee et al. 2020). Furthermore, Hoang et al. (2019) found that large grains will be disrupted and depleted around a very strong radiation source via a mechanism called RAdiative Torque Disruption (RAT-D; see Hoang 2020 for a review). The basic idea of the RAT-D mechanism is that an intense radiation field can spin up dust grains to extremely fast rotation, such that the centrifugal stress can exceed the tensile strength of the grain material, and so disrupts the dust grain into smaller fragments. The RAT-D effect is found to decrease the polarization fraction predicted by the RAT-A theory (Lee et al. 2020). It has been demonstrated that a combination of the RAT-A and RAT-D mechanisms can successfully reproduce the observed dust polarization data in various regions with strong radiation fields, such as Oph-A (Tram et al. 2021a) and 30 Doradus (Tram et al. 2021). Dust polarization observations toward strong radiation sources like M17 are therefore crucial to test grain alignment and disruption by RATs.

M17 is a well-known star-forming region (Povich et al. 2009; Lim et al. 2020) located in the Omega nebula or Swan nebula (also known as the Horseshoe nebula) in the constellation of Sagittarius at a distance $D = 1.98^{+0.14}_{-0.12}$ kpc. The distance to M17 was determined from the trigonometric parallaxes of methanol masers measured by the Very Long Baseline Array, which means the distance here is to the center of the active regions of high mass star formation within the cloud (Xu et al. 2011). Figure 1 is an RGB image of the region made using Spitzer[13] Galactic Legacy Infrared Midplane Survey Extraordinaire (GLIMPSE) mosaic data. Beside the study of B-fields and dust physics, since M17 is the closest giant H II region to Earth it is an excellent laboratory for the investigation of stellar feedback from a nearby massive star cluster and a photodissociation region (PDR), as well as from infrared sources in the regions such as UC 1, IRS 5, CEN 92, Anon 1, and Anon 3 (Lim et al. 2020). In this work, we use data taken by the High-resolution Airborne Wideband Camera Plus (HAWC+; Harper et al. 2018) accommodated on the Stratospheric Observatory for Infrared Astronomy (SOFIA; Temi et al. 2018).

The structure of the paper is organized as follows. The SOFIA/HAWC+ observations of M17 are presented in Section 2. In Section 3, we describe the use of the DCF method to estimate the B-field strengths. We then present our results, including the B-field morphologies and strengths, and discuss the implications of dust polarization fraction for grain alignment and disruption, in Section 4. A summary of our main findings is presented in Section 6.

2. Observations

Thermal dust polarization measurements of M17 were obtained using SOFIA/HAWC+ Band D, centered at a wavelength of 154 μm, with a beam size of $13''.6$. The observed region is shown in Figure 1. The maps have an original pixel size of $6''.9$ (Harper et al. 2018). Nyquist sampling was applied during the data reduction processes, resulting in final Stokes parameter maps with a resampled pixel size of $\sim 3''.4$. The Stokes I, Q, and U maps are shown in Figure 2.

The biased polarization fraction, $p_{\rm bias}$, is given by

$$p_{\rm bias} = 100\sqrt{\left(\frac{Q}{I}\right)^2 + \left(\frac{U}{I}\right)^2} = 100\frac{I_p}{I} \quad [\%] \qquad (1)$$

(Gordon et al. 2018), where $I_p = \sqrt{Q^2 + U^2}$ is the polarized intensity. The associated error on the biased polarization fraction is

$$\sigma_p = p_{\rm bias}\left[\left(\frac{\sigma_{I_p}}{I_p}\right)^2 + \left(\frac{\sigma_I}{I}\right)^2\right]^{1/2}, \qquad (2)$$

where σ_{I_p} and σ_I are the uncertainties on I_p and I, respectively. The error propagation on the nonlinear function $I_p(Q, U)$ is expanded as

$$\sigma_{I_p}^2 = \left|\frac{\partial I_p}{\partial Q}\right|^2 \sigma_Q^2 + \left|\frac{\partial I_p}{\partial U}\right|^2 \sigma_U^2 + 2\frac{\partial I_p}{\partial Q}\frac{\partial I_p}{\partial U}\sigma_{QU}. \qquad (3)$$

Assuming that Q and U are uncorrelated, i.e., the covariance term $\sigma_{QU} = 0$, we obtain the error on the polarized intensity

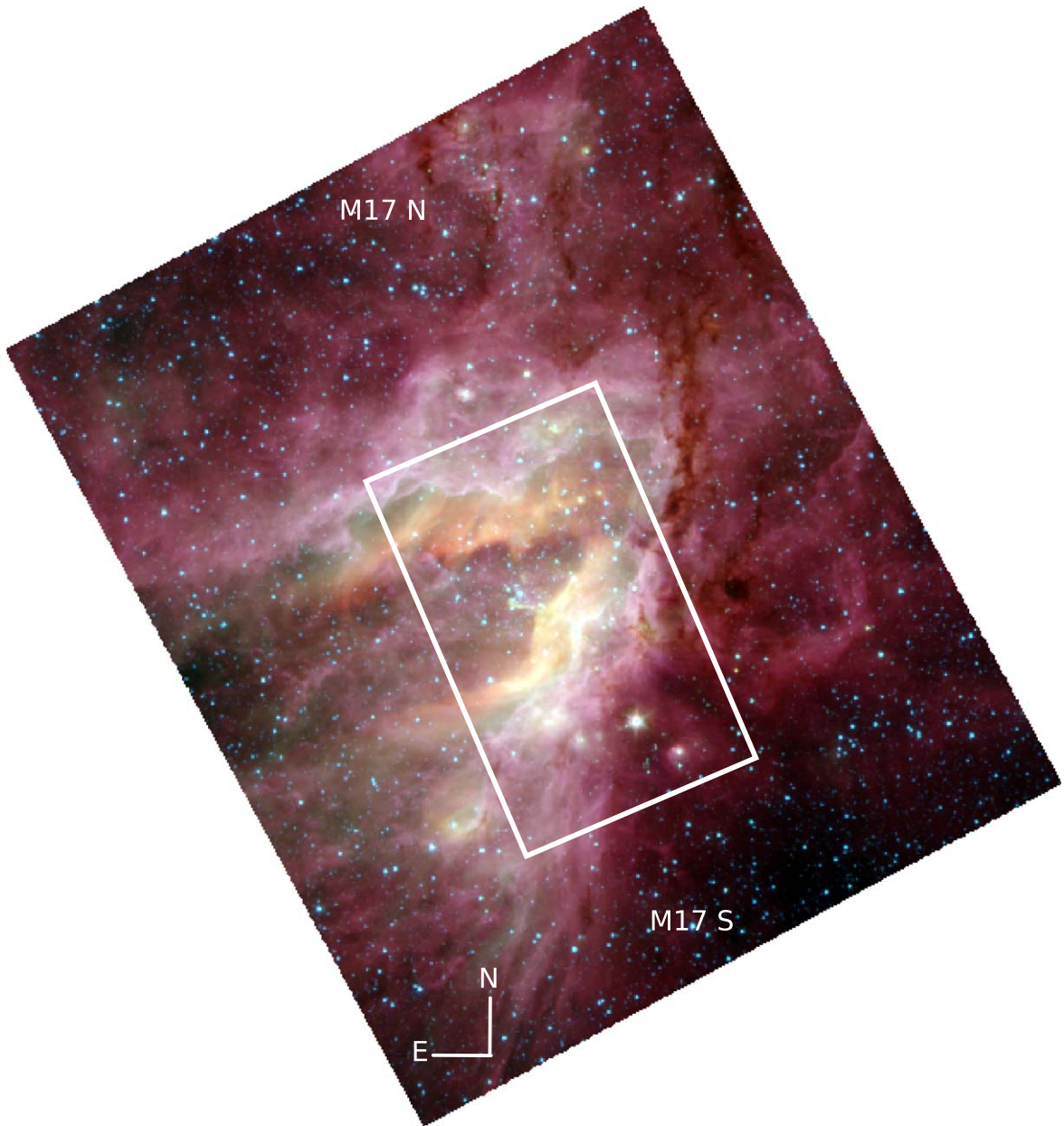$$\sigma_{I_p} = \left[\frac{Q^2\sigma_Q^2 + U^2\sigma_U^2}{Q^2 + U^2}\right]^{1/2}, \qquad (4)$$

---

[13] https://www.spitzer.caltech.edu

Figure 1. An RGB image of M17 observed by Spitzer ($R = 8$ μm, $G = 4.5$ μm, and $B = 3.6$ μm). The white rectangle shows the region observed by SOFIA/HAWC+ that is used in this work.

where σ_Q and σ_U are the errors on Stokes Q and U, respectively. The debiased polarization fraction, p, is calculated following the approach of Wardle & Kronberg (1974),

$$p = \sqrt{p_{\mathrm{bias}}^2 - \sigma_p^2}. \qquad (5)$$

The polarization angle, θ, is defined as

$$\theta = \frac{1}{2} \tan^{-1}\left(\frac{U}{Q}\right), \qquad (6)$$

and the error on the polarization angle is given by

$$\sigma_\theta = \frac{\sqrt{(Q\sigma_U)^2 + (U\sigma_Q)^2}}{2(Q^2 + U^2)}. \qquad (7)$$

A detailed exploration of the raw data is presented in the Appendix. In the following, we apply two quality cuts to the data, requiring a high signal-to-noise ratio (S/N) on the measurements of (1) the intensity $S/N_I > 236$ and (2) the polarization fraction $S/N_p > 3$. In what follows, we call this *master cut*. This quality cut automatically satisfies the third criterion recommended by the SOFIA Collaboration for high-quality scientific data, namely, $p < 50\%$ (Gordon et al. 2018). The cut on S/N_I is chosen such that measurement uncertainties on the polarization fraction, σ_p, are better than 0.6%. The approximate correlation between these two quantities is $S/N_I = \frac{\sqrt{2}}{\sigma_p} \approx 236$ (Gordon et al. 2018). After applying the master cut, 5139 pixels remain, corresponding to 23% of the original map, which has a size of 138×162 (22,356 pixels). The master cut excludes the low-level emission, and significantly improves the quality of the data. Its performance is illustrated in Figure A1 and Table A1. Subsequent analyses are carried out using this master cut.
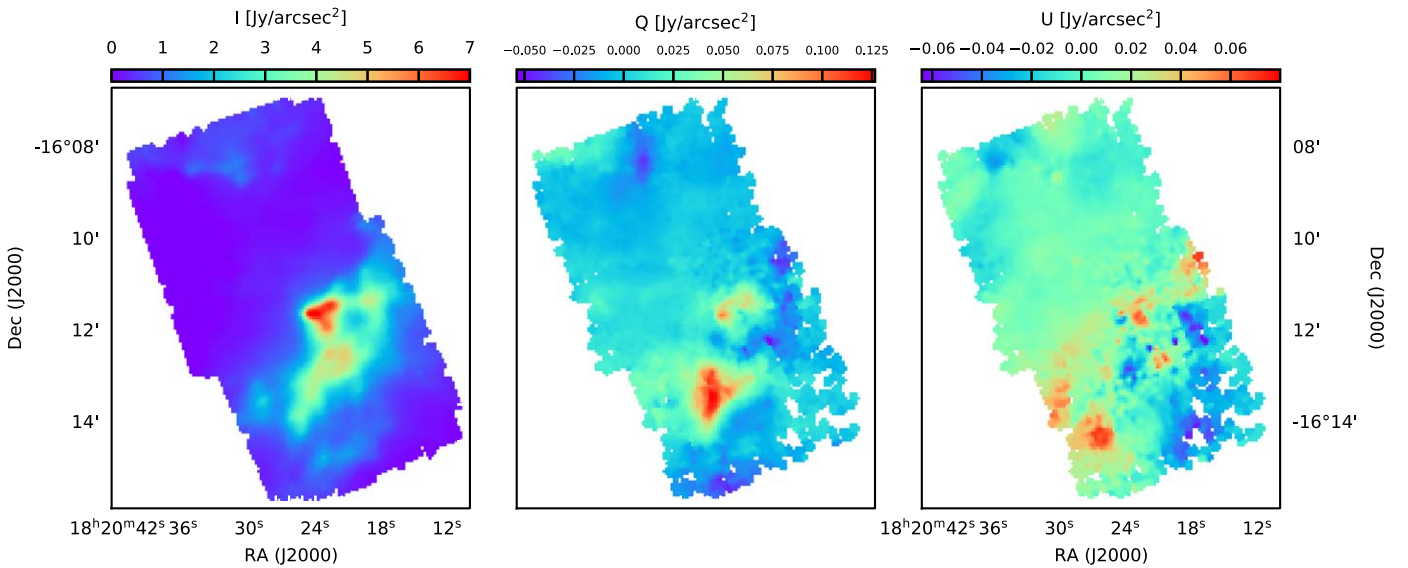
Figure 2. From left to right: SOFIA/HAWC+ 154 μm Stokes *I*, *Q*, and *U* maps of M17.

Figure 3 shows the inferred B-field orientation map of M17. The lengths of the line segments are proportional to the polarization fraction, and their orientations are obtained by rotating the polarization angles by 90° to trace the B-fields. The segments shown are called *half-vectors* since the directions of the vectors are not known. The map gives a first impression of the general B-field morphology of, and the polarization properties of the 154 μm emission from, the region.

3. Data Analysis

The DCF method is one of the most well-known techniques for estimating B-field strength. While there is some controversy around the method (e.g., Ostriker et al. 2001; Falceta-Gonçalves et al. 2008; Hildebrand et al. 2009; Pattle & Fissel 2019; Liu et al. 2021), the DCF method nonetheless provides a means by which to estimate B-field strength from dust polarization measurements. The method assumes that turbulent gas motions induce a turbulent B-field component on top of the mean, large-scale B-field in a region. If it is further assumed that these turbulence-induced perturbations are Alfvénic, the strength of the plane-of-sky component of the B-field, B_{POS}, can be calculated using the following equation (Crutcher 2004):

$$B_{POS} \; = \; Q_c \sqrt{4\pi\rho} \frac{\sigma_\nu}{\sigma_\theta} \approx 9.3 \sqrt{n(H_2)} \frac{\Delta V}{\sigma_\theta} \; [\mu G], \qquad (8)$$

where Q_c is a factor of the order of unity to correct for light-of-sight (LOS) and beam-integration effects, ρ is the gas density in grams per cubic centimeters, $\Delta V = \sigma_\nu \sqrt{8 \ln 2} = 2.355\sigma_\nu$ is the FWHM associated with the one-dimensional nonthermal gas velocity dispersion, σ_ν, in kilometers per second, $n(H_2)$ is the volume density of molecular hydrogen in cubic centimeters, and σ_θ is the polarization angle dispersion in degrees. In general, the magnetic field strength in MCs is in the range of micro to milligauss (e.g., Pattle & Fissel 2019).

The two ellipses shown on Figure 3 encompass two regions that are distinct both spatially and in terms of their physical conditions, including their density, temperature, and dynamics, as can be seen in Figures 5, 7, and 11 in the following sections.

The ellipse in the north is centered at R.A. $\sim 18^h20^m31^s.6$, decl. $\sim -16°08'04.''3$, with major × minor axes of $137'' \times 69''$, and a position angle of $14°$. The ellipse in the south is centered at R.A. $\sim 18^h20^m23^s.2$, decl. $\sim -16°12'24''$, with major × minor axes of $200'' \times 143''$, and a position angle of $0°$. We therefore divide the map into two corresponding northern and southern regions, which we name M17-N and M17-S, for further analyses. We will subsequently identify the input parameters for the DCF method in order to calculate the B-field strengths in the two regions.

3.1. Polarization Angle Dispersion: Structure Function

A longstanding problem in DCF studies is the separation of turbulence-induced dispersion from large-scale ordered variation in the B-field. If the latter were included, σ_θ would become unrealistically large. A number of methods have been proposed to account for the effect of ordered B-field variation (see, e.g., Pattle & Fissel 2019). We choose to adopt the structure function method of parameterizing the turbulent contribution to σ_θ.

The structure function method was initially proposed by Falceta-Gonçalves et al. (2008) and Hildebrand et al. (2009) as a means of evaluating the polarization angle dispersion, σ_θ, in the plane of sky. Fundamentally, this method calculates a two-point correlation function for pairs of polarization angles as follows:

$$\langle \Delta\theta(\ell) \rangle^{1/2} \; = \; \left\{ \frac{1}{N(\ell)} \sum_{i=1}^{N(\ell)} [\theta(\mathbf{x}) - \theta(\mathbf{x}+\ell)]^2 \right\}^{1/2}, \qquad (9)$$

where $\langle ... \rangle$ denotes an average; $N(\ell)$ is the number of pairs of pixels having a displacement between the two pixels of $|\ell| = \ell$; $\mathbf{x}$ and $\mathbf{x}+\ell$ are the location vectors of the two pixels under consideration, with corresponding polarization angles $\theta(\mathbf{x})$ and $\theta(\mathbf{x}+\ell)$, respectively. We note that only those pairs with $\Delta\theta(\ell) = |\theta(\mathbf{x}) - \theta(\mathbf{x}+\ell)| < 90°$ are retained for further analysis because the directions of the half-vectors are unknown. Assuming that the B-fields have two independent components—an ordered large-scale structure field component, B_0, and a turbulent field component, δB—for a small
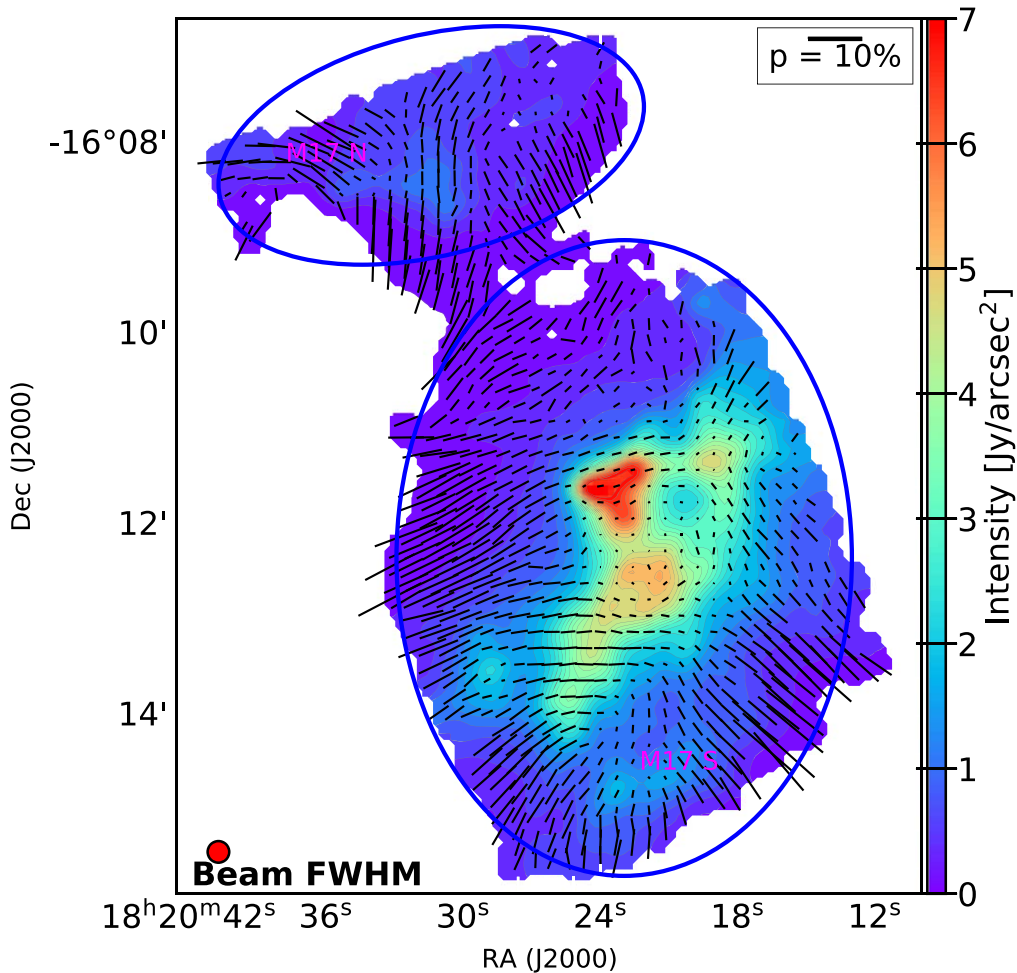
Figure 3. A map of the inferred B-field orientation in the M17 region observed by SOFIA/HAWC+. The half-vectors are proportional to the polarization fraction, and polarization angles are rotated by 90° to trace the B-fields. The color scale shows the total intensity in units of Jy arcsec^{-2}. The intensity map is smoothed with a kernel beam of 3×3 pixels. A line segment of 10% polarization is shown as a reference in the upper right corner. The beam size is shown in the lower left corner. The blue ellipses mark the M17-N and M17-S regions mentioned in the text.

displacement ℓ, the structure function can be written as (Hildebrand et al. 2009; Crutcher 2012)

$$\langle \Delta\theta(\ell) \rangle = b^2 + m^2\ell^2 + \sigma_M^2(\ell), \qquad (10)$$

where b is the contribution of turbulence, $m\ell$ is the contribution of the large-scale structure component, and $\sigma_M(\ell)$ represents the measurement uncertainties calculated for each pair of polarization angles. In practice, $\sigma_M(\ell)$ is taken into account while calculating $\langle \Delta\theta(\ell) \rangle^{1/2}$ in Equation (9). The ratio of the turbulent to large-scale structure components, and so of the angular dispersion resulting from turbulent motions, is expressed as (Hildebrand et al. 2009)

$$\sigma_\theta \simeq \frac{\delta B}{B_0} = \frac{b}{\sqrt{2 - b^2}}. \qquad (11)$$

The polynomial given in Equation (10), when fitted to the measured structure function, provides values of b and m. From Equation (11), for $b \ll 1$, $\sigma_\theta \simeq b/\sqrt{2}$ (where b is measured in radians).

We calculate the structure functions for M17-N and M17-S separately. The structure functions for both regions display similar rising tendencies at small displacements ℓ, reaching the expected dispersion of a random field of 52° at large

displacements (see Figure 4). The extent of M17-N is smaller than that of M17-S, hence the maximum displacement in M17-N is smaller. We then fit the measured structure functions as a function of ℓ using Equation (10). The fits were carried out for $\ell > 13''6$ to avoid attempting to fit structures below the beam size. The upper ℓ-limits were chosen to achieve the best fits to the smaller-scale structure (black curves in Figure 4). Table 1 lists the values obtained, particularly $b = 4°.9 \pm 0°.2$ and $8°.8 \pm 0°.7$, equivalent to $\sigma_\theta = 3°.5 \pm 0°.2$ and $6°.2 \pm 0°.5$ for M17-N and M17-S, respectively. The uncertainties on b are taken from the fitting procedure. We note these values are smaller than that found in M17 by Hildebrand et al. (2009), $\sigma_\theta \sim 10°$, using data from the Caltech Submillimeter Observatory at 350 μm with a spatial resolution of $\sim 20''$. Table 1 also lists the ratios of the turbulent and large-scale structure B-field components, calculated using Equation (11), which show that the turbulent field components are much smaller than the large-scale field components in M17.

3.2. Velocity Dispersion

We estimate the velocity dispersion in M17 using the publicly available archival ^{13}CO (J = 1 → 0) data taken using the Nobeyama 45 m telescope (Nakamura et al. 2019). The measurements were made at a central frequency of
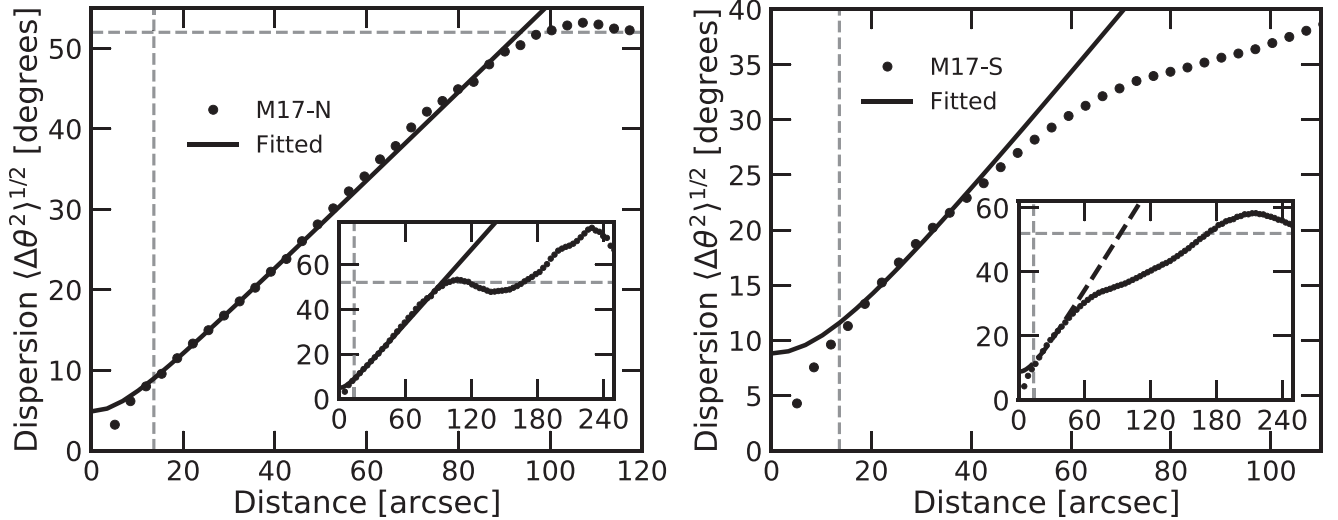
Figure 4. Structure functions $\langle \Delta \theta^2(\ell) \rangle^{1/2}$ for M17-N (left), and M17-S (right): black markers represent the data and black curves represent the fitted models. In the inserts, $\langle \Delta \theta^2(\ell) \rangle^{1/2}$ is shown for the full range of ℓ for each region. The horizontal dashed lines show the dispersion predicted for a random field, $\pi/\sqrt{12} \sim 52°$ (Serkowski 1962; Planck Collaboration et al. 2015). The vertical dashed lines show the SOFIA/HAWC+ beam size of $13.6''$ at $154~\mu$m.

Table 1
A Summary of the Results Obtained for Our DCF Analysis

Parameters	M17-N	M17-S
b	4.9 ± 0.2	8.8 ± 0.7
m	0.55 ± 0.002	0.55 ± 0.01
$\delta B/B_0$	0.06	0.11
Polarization angle dispersion, σ_θ [deg]	3.5 ± 0.2	6.2 ± 0.5
Peak position, ν_{LSR} [km s^{-1}]	22.7 ± 0.1	19.9 ± 0.1
Velocity dispersion, $\sigma_{\nu,^{13}\mathrm{CO}}$ [km s^{-1}]	1.6 ± 0.1	2.3 ± 0.1
Column density, $\langle N(\mathrm{H}_2) \rangle$ [cm^{-2}]	$(9.1 \pm 4.0) \times 10^{21}$	$(6.2 \pm 6.5) \times 10^{22}$
Volume density, $n(\mathrm{H}_2)$ [cm^{-3}]	$(9.3 \pm 4.1) \times 10^3$	$(4.2 \pm 4.4) \times 10^4$

Note. b is the rms contribution of the turbulent B-field component to the polarization angle dispersion, σ_θ, and m is the contribution of the large-scale B-field to σ_θ. $\delta B/B_0$ is the ratio of the turbulent to the large-scale field components. Detailed descriptions of the parameters can be found in the text.

$\nu_{\mathrm{central}} \sim 110.201$ GHz, with a spectral resolution of 0.1 km s^{-1}. The resulting map has a pixel size of $7.5''$ and a beam size of $14.9''$. We cropped this map to match the region of M17 observed by SOFIA/HAWC+. Figure 5 presents the velocity-integrated intensity (left) and mean velocity (right) maps. The integration was performed over the entire velocity range from -20 to 60 km s^{-1} in the local standard of rest (LSR) frame. Figure 6 displays the integrated spectra averaged over M17-N (left) and M17-S (right). The spectra can both be well described by two-Gaussian fits, which give the mean positions and corresponding standard deviations, $\sigma_{\nu,^{13}\mathrm{CO}}$, of the two velocity components. The spectra of M17-N and M17-S show main peaks at 22.7 ± 1.6 and 19.9 ± 2.3 km s^{-1}, respectively. These main peaks are much brighter than the secondary components. Therefore, we only use the velocity dispersions of these two peaks in our calculation of the B-field strengths in M17-N and M17-S. Table 1 summarizes the results of the fits, which are in agreement with the results obtained by Nakamura et al. (2019) and Nguyen-Luong et al. (2020), although their results are for

wider areas of M17. The statistical uncertainties on the velocity dispersions from the two-Gaussian fits are smaller than the spectral resolution of Nobeyama; therefore, we take the uncertainties to be equal to the spectral resolution, 0.1 km s^{-1}. We note that M17-N is affected by the outflows and shocks from G015.128[14] (Lim et al. 2020), which is expected to be more turbulent than M17-S.

The measured velocity dispersions are then converted to nonthermal velocity dispersions using $\sigma_\nu^2 = \sigma_{\nu,^{13}\mathrm{CO}}^2 - \dfrac{k_\mathrm{B} T}{m_{^{13}\mathrm{CO}}}$, where $m_{^{13}\mathrm{CO}}$ is the ^{13}CO molecule mass, equal to 29 amu, k_B is the Boltzmann constant, and T is the gas temperature. The thermal contribution to the velocity dispersion is negligible if we adopt an average gas temperature of 20 K (Nguyen-Luong et al. 2020). Therefore, we take the nonthermal velocity dispersion for the M17-N and M17-S regions to be equal to the standard deviations of their respective main peaks, as listed in Table 1.

3.3. Column and Volume Densities

The column density, $N(\mathrm{H}_2)$, has been derived using a graybody (i.e., modified blackbody) fit to Herschel Space Observatory data, combining the filter-weighted opacity, κ_ν, and the Planck function for blackbody radiation, $B_\nu(T_\mathrm{d})$. Following the techniques described by Lim et al. (2016), we convolved the Herschel 160, 250, and 350 μm observations of M17 to the beam size of the Herschel 500 μm images ($\sim 36''$), before performing pixel-by-pixel graybody fitting to all four bands of data. The template T_d, with an angular resolution of $\sim 36''$ was re-gridded to match to the pixel geometry of the SCUBA-2 850 μm map of M17 (Reid & Wilson 2006; angular resolution $\sim 14''$ and pixel size $4''$). We then repeated the graybody fit by combining the SCUBA-2 850 μm map with the re-gridded T_d map to solve for $N(\mathrm{H}_2)$. Figure 7 shows the resulting $N(\mathrm{H}_2)$ map, with contours of dust temperature superimposed. (Dust temperatures are shown in Figure 11.)

---

[14] G015.128 is a massive young stellar object, and likely an A-type supergiant star (Pomohaci et al. 2017). The current SOFIA/HAWC+ data do not fully cover this source.
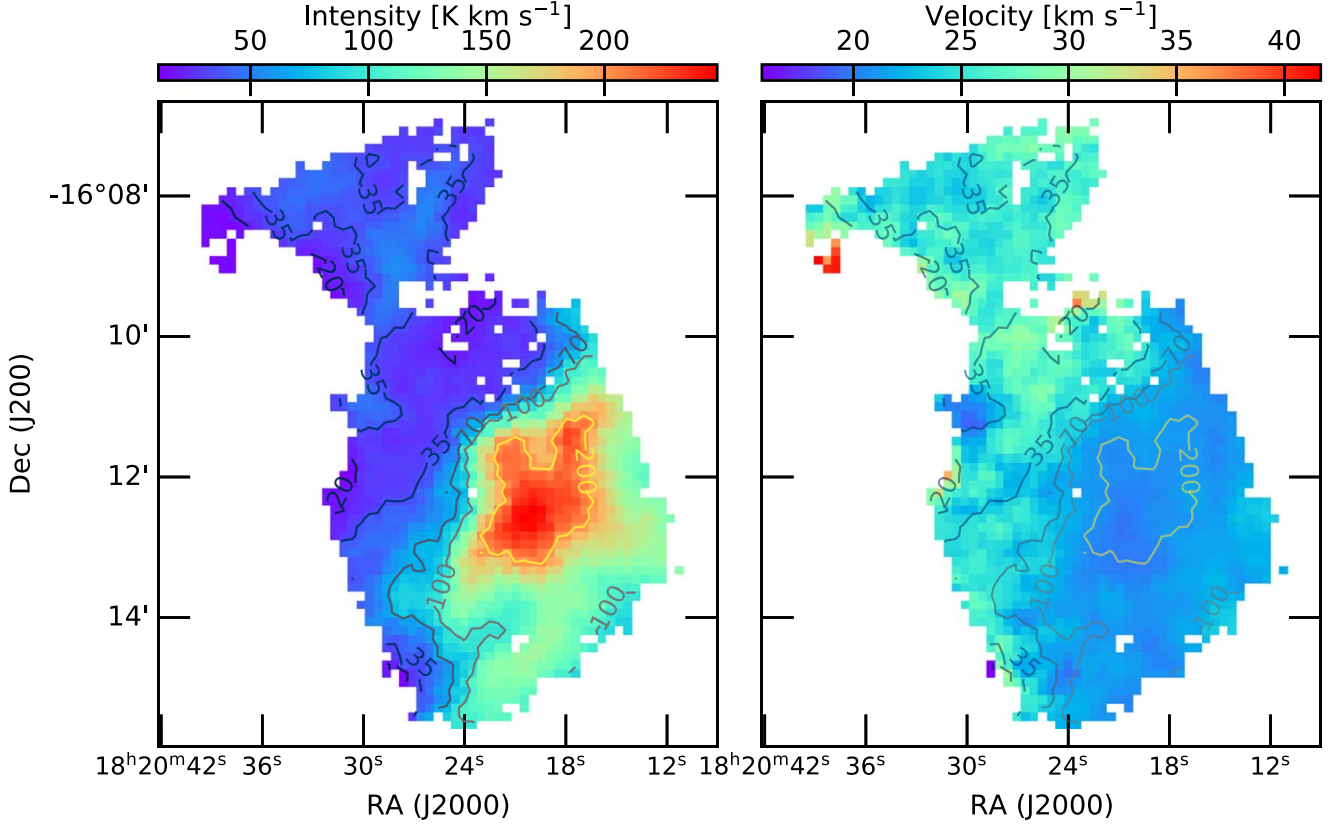
Figure 5. Left: velocity-integrated Nobeyama 45 m telescope ^{13}CO (J = 1 → 0) intensity map. Right: mean velocity map. The contour levels are at 20, 35, 70, 100, and 200 K km s^{-1} for both maps.

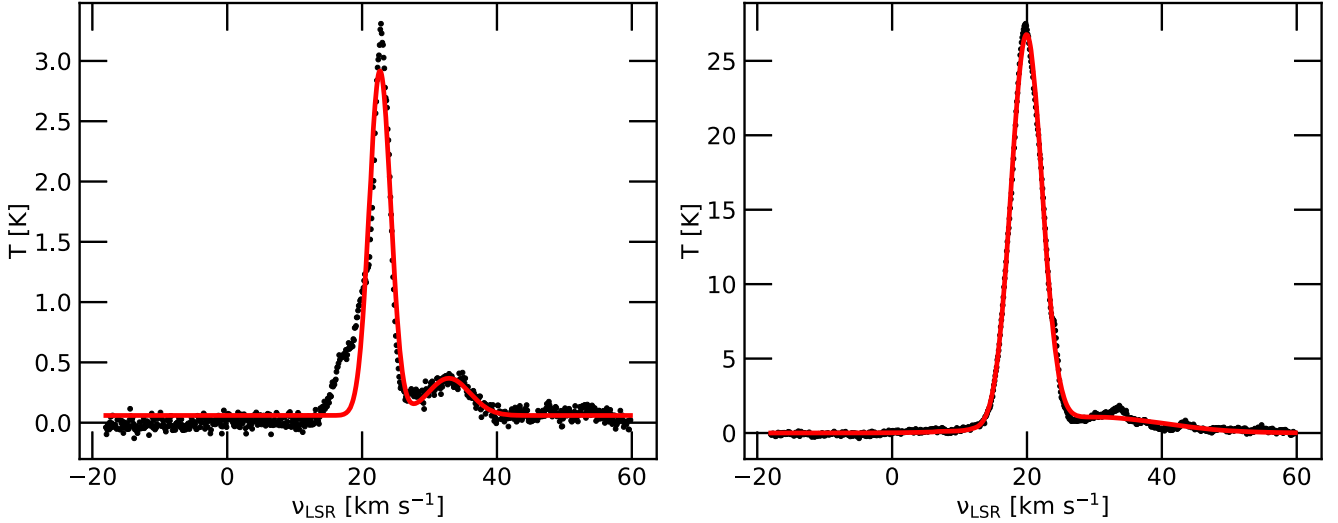**Figure 6.** Average integrated Nobeyama 45 m telescope ^{13}CO (J = 1 → 0) spectra (black) with two-Gaussian fits (red) for M17-N (left) and M17-S (right).

Using this map, we calculate the total column densities, $N_{\text{total, H}_2}$ and the average column densities $\langle N(\text{H}_2) \rangle$, as well as their associated uncertainties $\sigma_{N(\text{H}_2)}$, for the M17-N and M17-S regions. These results are presented in Table 1.

We then follow the approach described by Lee et al. (2012), Li et al. (2014), and Ngoc et al. (2021) to estimate the volume density, $n(\text{H}_2)$. The mass of a region is given by $M = \beta m_{\text{H}_2} N_{\text{total,H}_2} (D\Delta)^2$, where $\beta = 1.39$ accounts for a He abundance of 10% in addition to H$_2$ in the total mass, m_{H_2} is the mass of a hydrogen molecule, $D = 1.98$ kpc is the distance

to M17 (Xu et al. 2011), and $\Delta = 4''$ is the pixel size of the $N(\text{H}_2)$ map. Then the volume density $n(\text{H}_2)$ is given by

$$n(\text{H}_2) = \frac{3M}{4\pi R^3 m_{\text{H}_2}} = \frac{3\beta N_{\text{total,H}_2}(D\Delta)^2}{4\pi R^3} \quad [\text{cm}^{-3}], \quad (12)$$

where R is the effective radius of the clump under consideration, equal to $R = \sqrt{(ab)/2}$, and a and b are the major and minor axes of an ellipse covering the clump (Li et al. 2014). Equation (12) is deduced assuming that the clump of molecular
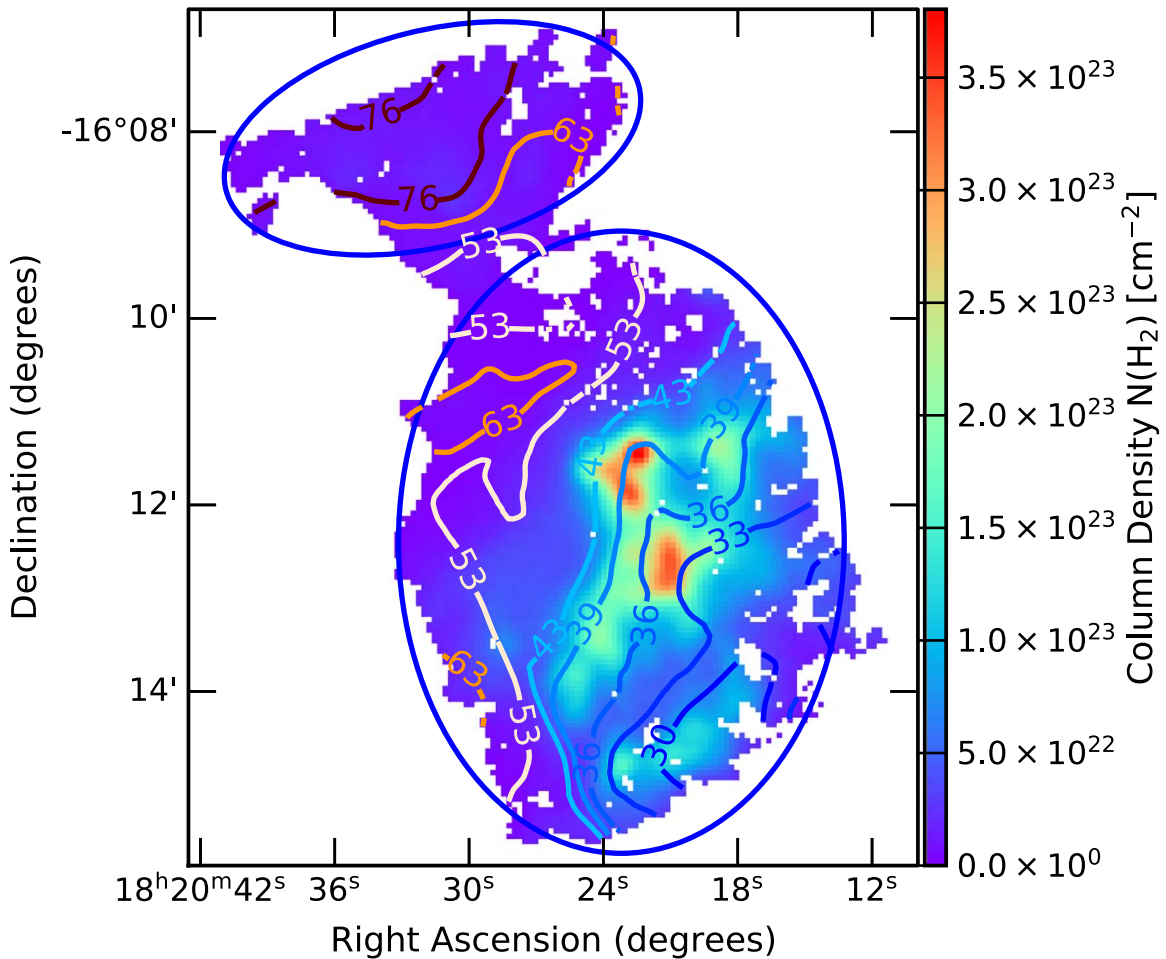
Figure 7. Map of the column density, $N(H_2)$, of M17. The contours display the dust temperature (T_d) values, as shown in Figure 11. The blue ellipses are the same as those in Figure 3. In M17-S, the relation between T_d and $N(H_2)$ is complex. T_d is positively correlated with $N(H_2)$ up to ~ 43 K, but is negatively correlated beyond this temperature.

gas has a spherical geometry. As shown in Figures 3 and 7, we define two ellipses that encompass the observed M17-N and M17-S regions, with angular radii of 69″ and 120″, respectively. The physical radii of the two clumps are given by $R \times D$. The $n(H_2)$ values calculated for M17-N and M17-S using Equation (12) are shown in Table 1. The uncertainty on $n(H_2)$ is calculated assuming that its fractional uncertainty is the same as that of N_{total,H_2}, i.e., $\frac{\sigma_{n(H_2)}}{n(H_2)} = \frac{\sigma_{N(H_2)}}{\langle N(H_2) \rangle}$.

4. Results

In this section, we first describe the magnetic field morphology of M17, and report on the plane-of-sky B-field strengths measured using the DCF method in M17-N and M17-S. We then explore the relative contribution of B-fields, gravity, and turbulence by calculating mass-to-flux ratios and Alfvénic Mach numbers for the two regions.

4.1. Magnetic Field Morphology

The morphology of interstellar magnetic fields is imprinted onto star formation processes. We can thus use our observational data to test theoretical predictions of the role of magnetic fields in star formation.

Over M17 as a whole, B-fields in the outer, low-density regions are perpendicular to the density structure. Figure 3 and its close-up version (Figure A3) illustrate this point well, with many half-vectors in the low-density regions being orthogonal to the intensity contours. Another prominent feature is that when the field lines pass through the H II region, on the eastern side of the observed region, they tend to run parallel to the major axes of both M17-N and M17-S, threading the space between them (see Figure 1 of Povich et al. 2009 for a more precise location of the H II region). However, in the high-density areas at the center of M17-S, the fields run perpendicular to those running through the H II region (see Figure 8).

In the M17-N region, the B-field mainly run in a north–south direction through the highest-density area, curving in the eastern and western sides of the region (see Figures 8 and A3). The morphology of the B-fields in M17-N mimics the field of a gravitationally collapsing molecular core in the presence of strong magnetic fields, where we see the classical hourglass geometry, with a linear field in the center and curved fields in the two wings. This is a common structure which is often found in observations and simulations (see, e.g., Kandori et al. 2018; Wurster & Li 2018; Pattle & Fissel 2019). However, M17-N is only a small part of a much larger M17-N region (see Figure 9), which is not fully covered by the current SOFIA/HAWC+
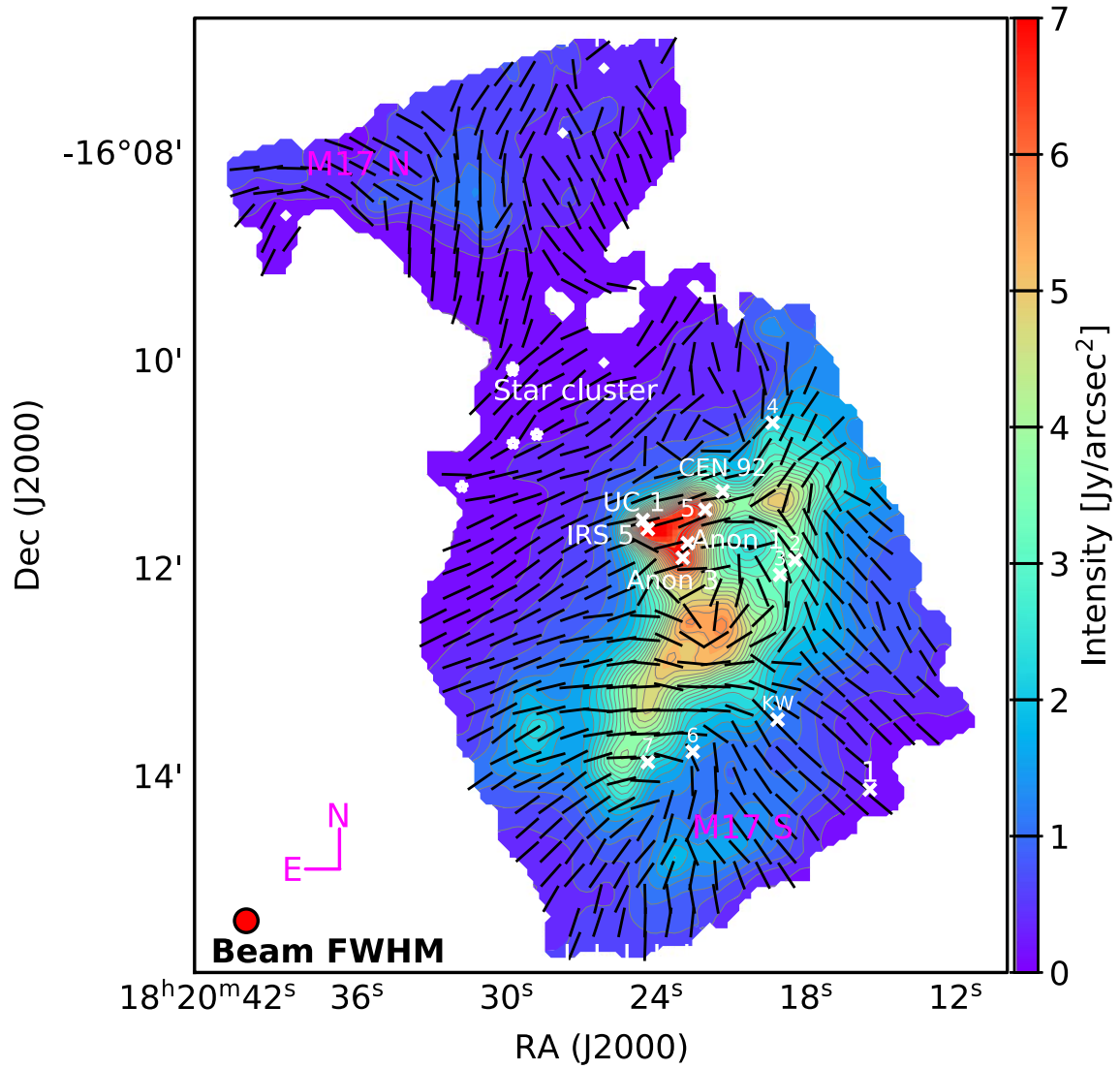
Figure 8. B-field morphology of M17 superimposed on the intensity map. Half-vectors show polarization angles rotated by 90°, representing the magnetic field orientation, and are plotted with uniform length. The star symbols mark the most massive (>O7) stars in the open cluster NGC 6618 (Hanson et al. 1997). There are several infrared sources present in M17-S, including UC 1, IRS 5, CEN 92, Anon 1, and Anon 3. The Kleinmann–Wright (KW) object is a binary-star system Kleinmann & Wright (1973). The locations of the sources are taken from Lim et al. (2020).

observations. Therefore, the observed structure may be just a coincidence, with the fields following the emission by polycyclic aromatic hydrocarbons observed by Spitzer at a wavelength of 8 μm (the bright pink-colored structure in the northern region of Figure 9). Distinguishing these two scenarios requires observations at higher angular resolution and of larger areas of M17-N.

In the M17-S region, the fields generally run perpendicular to the elongation of the high-density structure. The fields also form an asymmetric large-scale hourglass shape in the region (see Figures 8–10). In the southern side of the hourglass, just below Anon 1 and Anon 3, the fields run from east to west while gradually bending to the south. The fields are highly curved in the most southern part of the region, and are perturbed in the high-density regions in its center. On the northern side of the hourglass, just above UC 1 and CEN 92, we see curved fields (see Figures 8 and 10). This hourglass structure seems to be clearly caused by the gravitational contraction of the massive cores at the center of M17-S.

Moreover, the asymmetry is due to the complex distribution of matter in the center and northwestern part of the region. Another prominent feature of M17-S, which is commonly found in PDR regions (see, e.g., Pattle et al. 2018), is the pillar structure. Here we find a *triangular* pillar, with the top end coincident with the positions of UC 1 and IRS 5 and a *base* to the west (see Figures 8 and 10). It is interesting to note that the magnetic field morphology found here is similar to those reported by Pattle et al. (2018), with the fields running parallel to the pillar beside the H II region, and perpendicular to the pillar in and behind its base.

Dotson (1996) reported that magnetic field lines in M17 are elongated into the cloud core and bulge away from the H II region, which is heated by OB stars. This could be evidence that the H II region is expanding into its surrounding medium (Zeng et al. 2013). In conclusion, our observed magnetic field morphology is consistent with the scenario in which the magnetic field is distorted by the H II region (discussed further in Section 5.1), several IR sources, and stellar clusters.
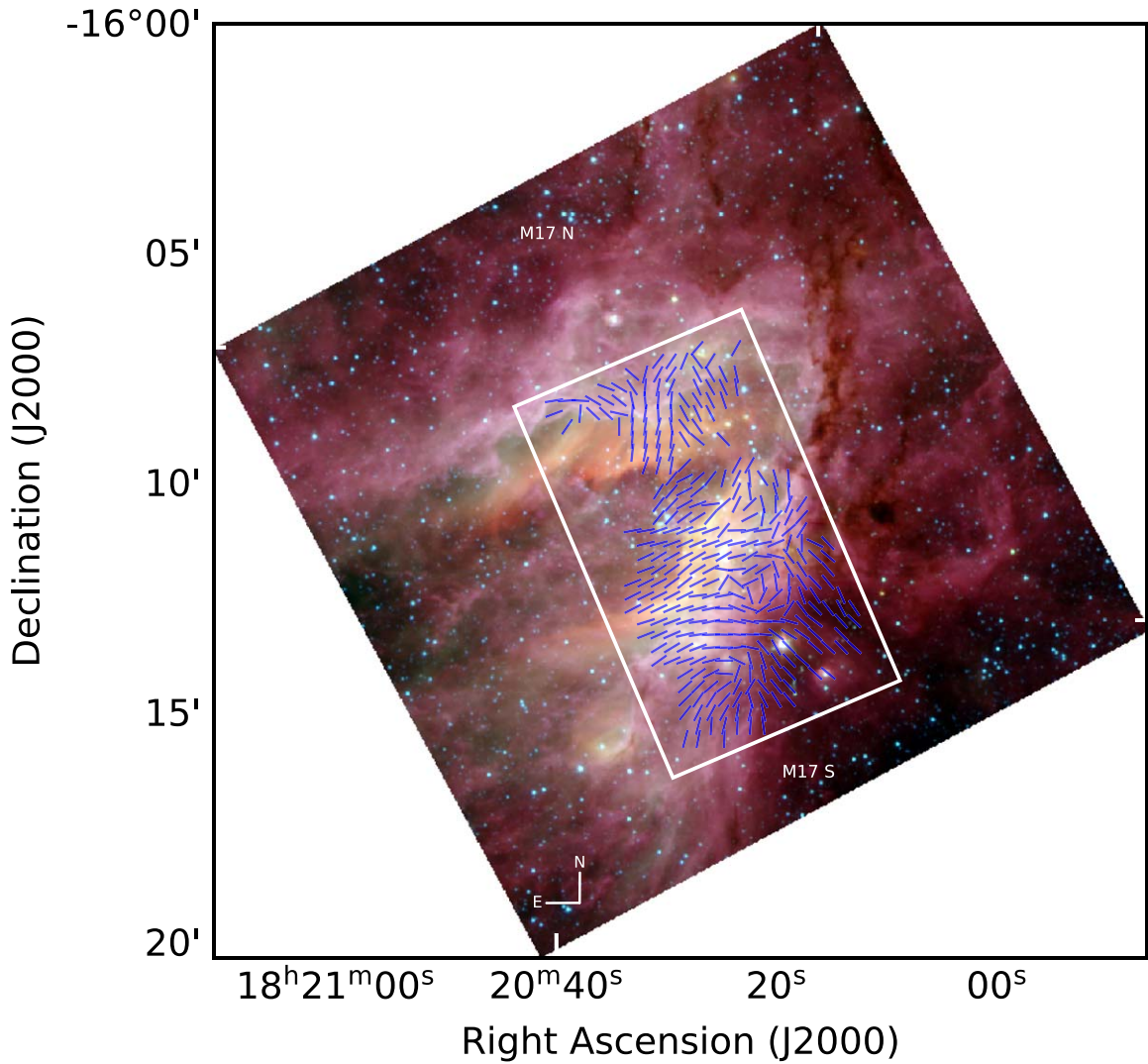
Figure 9. An RGB image of M17 using Spitzer data, as described in Figure 1. The white box marks the area of M17 observed by SOFIA/HAWC+. The half-vectors show SOFIA/HAWC+ data, and are plotted with uniform length and rotated by 90° to trace the magnetic field direction. In this figure, we can see the larger-scale structure connected to the M17-N region, which is described in the text.

4.2. Magnetic Field Strengths

We calculate the plane-of-sky B-field strength using Equation (8) and the estimated values of σ_θ, σ_ν and $n(H_2)$ listed in Table 1, yielding $B_{POS} = 980 \pm 230$ and $1665 \pm 885 \, \mu G$ for M17-N and M17-S, respectively (more details are given in Table 2). The greater magnetic field strength measured in M17-S than in M17-N results from its higher density.

We note that the DCF method is applicable in this case since both of the measured polarization angle dispersions are smaller than 25° (Crutcher 2004). The uncertainties are propagated from the uncertainties on σ_θ, σ_ν, and $n(H_2)$ using

$$\frac{\delta B_{POS}}{B_{POS}} = \sqrt{\left(\frac{1}{2}\frac{\delta n(H_2)}{n(H_2)}\right)^2 + \left(\frac{\delta \Delta V}{\Delta V}\right)^2 + \left(\frac{\delta \sigma_\theta}{\sigma_\theta}\right)^2}, \quad (13)$$

where $\delta n(H_2)$, $\delta \Delta V$, and $\delta \sigma_\theta$ are the uncertainties on σ_ν, $\Delta V = 2.355\sigma_\nu$, and σ_θ, respectively.

A study by Pellegrini et al. (2007) found the magnetic field strength around the southwestern part of the M17 photodissociation region to have a peak value of $\sim 600 \, \mu G$. Brogan et al. (1999) directly measured the magnitude of the

B-fields along the LOS using observations of Zeeman splitting of H I absorption lines toward the H II region, obtaining $B_{LOS} \sim -450$ to $550 \, \mu G$. Chen et al. (2012) carried out a rough estimate of the magnetic field strength from the polarization of point sources in the near-IR and far-IR using a sampling rectangle in the M17-S region. They found a total magnetic field strength of $B = \sqrt{B_{LOS}^2 + B_{POS}^2} \sim 230 \, \mu G$, and an inclination angle of the magnetic field vector with respect to the plane of the sky of $\sim 40°$. Our estimated values of $B_{POS} = 980 \pm 230$ and $1665 \pm 885 \, \mu G$ are therefore, within their rather large uncertainties, comparable to previous results.

Several factors affect our estimate of the magnetic field strengths. One is our assumption of spherical geometries for the molecular clumps in order to estimate the radii of the observed regions when estimating the volume densities. Depending on the true 3D geometries of the clouds, this assumption could lead to a large uncertainty in B_{POS} values. In addition, polarization observations integrate over all of the structure along the LOS, which leads to a reduction in σ_θ, and therefore, to an overestimate of B-field strengths. It is also important to note that, statistically, the margin by which the DCF method
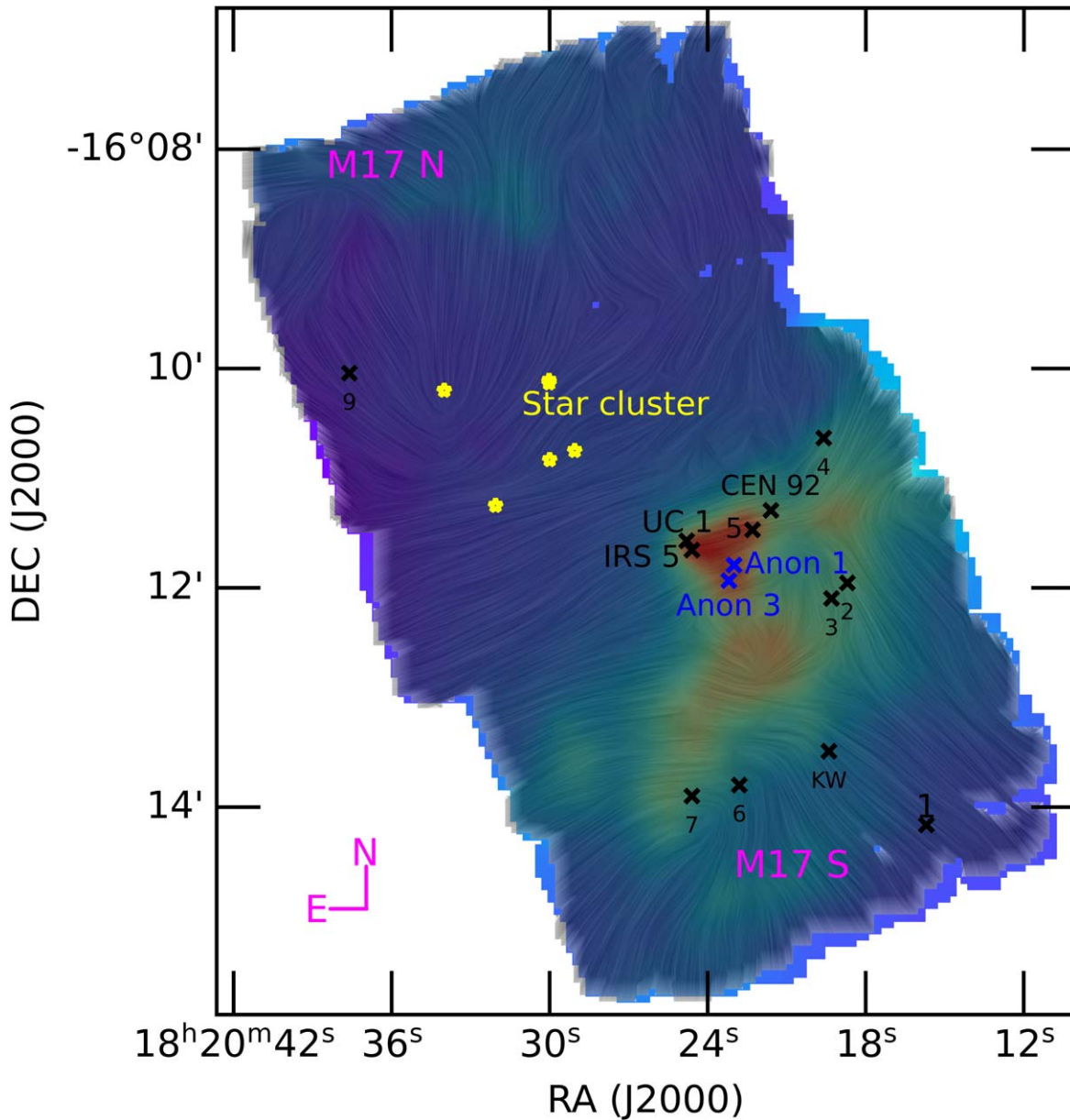
Figure 10. Same as Figure 8, but with the magnetic field observed by SOFIA/HAWC+ represented using a *drapery* pattern produced by the line integral convolution (LIC) tool (Cabral & Leedom 1993).

Table 2
Measured Magnetic Field Strengths, Alfvénic Mach Numbers and Mass-to-flux Ratios for M17-N and M17-S

Region	B_{POS} [μG]	Mach Number $\mathcal{M}_A$	Mass-to-flux Ratio λ
M17-N	980 ± 230	$0.12 \sin \gamma$	0.07 ± 0.04
M17-S	1665 ± 885	$0.22 \sin \gamma$	0.28 ± 0.33

Note. γ is the inclination angle of the B-fields with respect to the LOS.

overestimates magnetic field strengths can be up to a factor of 2 for an individual cloud (Crutcher 2004). There are efforts to improve the DCF method, such as those of Cho & Yoo (2016), who modified the method to reduce the overestimate of B_{POS} strength by a factor equal to the ratio of the average LOS velocity dispersion and the standard deviation of centroid

velocities. We calculated the standard deviation of centroid velocities for the M17-N and M17-S regions to be 0.59 and 1.46 km s^{-1}, respectively. This suggests that the conventional DCF method overestimates the strength of the mean magnetic field in the plane of the sky by a factor of $(1.6/1.46) = 1.1$ and $(2.3/0.59) = 3.9$ in M17-N and M17-S, respectively (the LOS velocity dispersion is taken from Table 1). The B-field strengths therefore become 891 ± 209 and 427 ± 227 μG for M17-N and M17-S, respectively.

Our calculated B-field strengths have quite large uncertainties, which are mostly propagated from the uncertainties on column densities averaged over large regions (see the results in Table 1). We therefore examine the B-field strength in only the highest-density regions, with $N(H_2) > 10^{22}$ cm^{-2}. With this new cut, only the densest regions of M17-S are retained (see Figure A4) and the new results are $N(H_2) = (7.6 \pm 6.5) \times 10^{22}$ cm^{-2} and $n(H_2) = (6.9 \pm 5.9) \times 10^4$ cm^{-3}, while $\Delta V = (2.3 \pm 0.1)$ km s^{-1}

and $\sigma_\theta = 6°\!.5 \pm 0°\!.5$ are the same as before the new cut was applied. Therefore, the magnetic field strength obtained is $B_{\mathrm{POS}} = 2134 \pm 738\,\mu\mathrm{G}$ and $\lambda = 0.27 \pm 0.25$, with smaller uncertainties as expected. This calculation serves as a reference providing a more precise measurement of the average magnetic field strength in the densest region of M17, and a sense of possible changes of its value depending on how the regions of interest are chosen. In reality, the magnetic field strength is expected to change with the local gas density.

4.3. Alfvénic Mach Number $\mathcal{M}_\mathcal{A}$

The Alfvénic Mach number, $\mathcal{M}_\mathcal{A}$, represents the relative contribution of turbulence to magnetic fields. $\mathcal{M}_\mathcal{A}$ is an important parameter for describing the evolution of MCs (Kritsuk et al. 2017). A sub-Alfvénic value ($\mathcal{M}_\mathcal{A} < 1$) means the cloud has a strong magnetic field, while a super-Alfvénic value ($\mathcal{M}_\mathcal{A} > 1$) implies a weak magnetic field compared to turbulence. In the super-Alfvénic case, the magnetic field morphology is significantly affected by turbulence, due to its subdominance. In this scenario, the morphology of the magnetic field is therefore expected to be random.

$\mathcal{M}_\mathcal{A}$ can be calculated from the velocity dispersion, following Padoan et al. (2001), Nakamura & Li (2008), and Wang et al. (2019), as

$$\mathcal{M}_\mathcal{A} = \frac{\sigma_\nu}{v_A} = \frac{\sigma_\nu\sqrt{4\pi\rho}}{B}, \qquad (14)$$

where v_A is the Alfvénic velocity. Combining with Equation (8), we obtain

$$\mathcal{M}_\mathcal{A} = \frac{\sigma_\theta \sin\gamma}{Q_c}, \qquad (15)$$

where γ is the inclination angle of the B-field with respect to the LOS, in the range [0°, 90°], with $B_{\mathrm{POS}} = B \sin\gamma$ and $Q_c = 0.5$ (Ostriker et al. 2001).

Using the inferred dispersion in polarization angle given in Table 1, we obtained $\mathcal{M}_\mathcal{A} = 0.12 \sin\gamma$ and $0.22 \sin\gamma$ for M17-N and M17-S, respectively. Thus, M17 is sub-Alfvénic, implying that the magnetic fields in the region dominate over turbulence. These sub-Alfvénic Mach numbers are also in agreement with the generally well-ordered magnetic field morphology in the region (see Figure 8).

4.4. Mass-to-flux Ratio

The ratio of mass-to-magnetic flux, M/Φ (generally referred to as the mass-to-flux ratio), is a crucial parameter describing the importance of B-fields relative to gravity in star formation (Crutcher 2012). It is usually given in terms of its critical value,

$$\lambda = \frac{(M/\Phi)_{\mathrm{observed}}}{(M/\Phi)_{\mathrm{critical}}} = 7.6 \times 10^{-21} \frac{\langle N(\mathrm{H}_2)\rangle}{B_{\mathrm{POS}}}, \qquad (16)$$

(Crutcher 2004), where the critical mass-to-flux ratio $(M/\Phi)_{\mathrm{critical}} = \frac{1}{2\pi\sqrt{G}}$ (Nakano & Nakamura 1978), $\langle N(\mathrm{H}_2)\rangle$ is the average column density of the region under consideration in units per square centimeter, and B_{POS} is given in units of microgauss. We note that an analysis by Crutcher (2004) indicated that, statistically, the true mass-to-flux ratio may be overestimated by a factor of three. The errors on the mass-to-

flux ratio are given by

$$\frac{\sigma_\lambda}{\lambda} = \sqrt{\left(\frac{\sigma_{N(\mathrm{H}_2)}}{\langle N(\mathrm{H}_2)\rangle}\right)^2 + \left(\frac{\delta B_{\mathrm{POS}}}{B_{\mathrm{POS}}}\right)^2}. \qquad (17)$$

A supercritical value of $\lambda > 1$ means that gravity dominates over magnetic pressure, and so the cloud can undergo gravitational collapse to form a protostar. Conversely, a subcritical value of $\lambda < 1$ indicates that the magnetic field is strong enough to counteract gravitational collapse (Crutcher 2004; Pattle et al. 2017).

We obtained $\lambda = 0.07$ and 0.28 for the M17-N and M17-S regions, respectively (see Table 2). Overall, the M17 cloud is subcritical, meaning that M17 is magnetically supported and belongs to the strong magnetic field model of star formation theory (Nakano & Nakamura 1978). However, the λ values here are calculated by averaging over the whole of the regions considered. Therefore, the highest-density cores can still become supercritical and then gravitationally collapse to form new stars. The inferred values of the mass-to-flux ratio are compatible with theoretical predictions of the ambipolar diffusion model in which the B-field is dragged inward from the outer layers of the cloud to the massive cores in both M17-N and M17-S. In addition, these results are compatible with the deficiency of forming massive stars and the lack of gravitationally bound clumps in the regions (Nguyen-Luong et al. 2020).

5. Discussion

In this section, we discuss the stellar feedback from the star cluster and the dust temperature of the region. We then investigate dust grain alignment and disruption in the region that we have observed, using the relations between polarization fraction and emission intensity, column density, and dust temperature.

5.1. Stellar Feedback from the Massive Star Cluster

As shown in Figures 8 and 10, the magnetic fields in the vicinity of the star cluster (yellow symbols in Figure 10) appear to be bent and aligned with the density structure (see, e.g., Section 4.1). This suggests the effects of stellar feedback from the massive star cluster on the magnetic field.

To understand the importance of feedback, we estimate the ratio of the ram pressure, P_{ram}, due to stellar winds (or to expansion of the H II region) to the magnetic pressure, P_{mag}, which is given by

$$\frac{P_{\mathrm{ram}}}{P_{\mathrm{mag}}} = \frac{\rho v_{\mathrm{wd}}^2}{B^2/8\pi}$$

$$\simeq 4.7\left(\frac{v_{\mathrm{wd}}}{20\ \mathrm{km\,s^{-1}}}\right)^2\left(\frac{1000\ \mu\mathrm{G}}{B}\right)^2\left(\frac{n(\mathrm{H}_2)}{10^4\ \mathrm{cm^{-3}}}\right), \qquad (18)$$

where the wind speed $v_{\mathrm{wd}} \sim 20\,\mathrm{km\,s^{-1}}$ is adopted from Pellegrini et al. (2007), a study of magnetic support in the M17 PDR. The mass density, ρ, is given by $\rho = 2.8 m_{\mathrm{H}} n(\mathrm{H}_2)$. Volume densities, $n(\mathrm{H}_2)$, and magnetic field strengths, B, close to those listed in Tables 1 and 2 have been used. The dominance of the ram pressure over the magnetic pressure, $P_{\mathrm{ram}}/P_{\mathrm{mag}} \sim 4.7$, as shown in Equation (18), implies that the
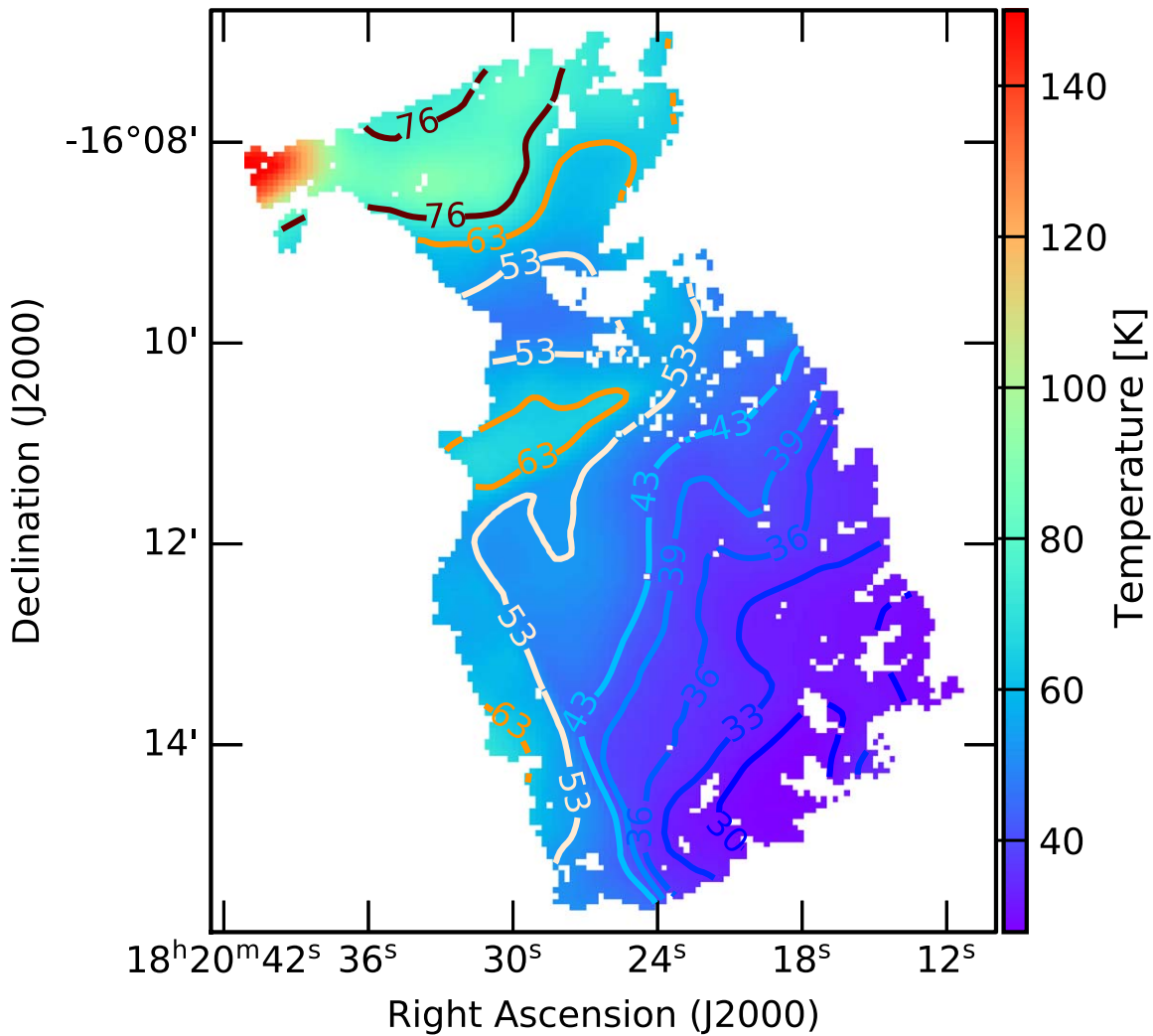
Figure 11. Dust temperature map of M17, with selected contours of constant temperature marked. In M17-S, the dust temperature tends to decrease from east to west, in the direction leading away from the star cluster.

winds can bend the magnetic fields that are frozen into the gas. Stellar feedback from the star cluster may also trigger star formation in the M17-S region, as revealed by the presence of numerous IR sources.

5.2. Dust Temperature Map

As described in Section 3.3, the dust temperature, T_d, map has been derived from graybody fits to Herschel 160–500 μm data. Then, the template T_d map has been re-gridded to match the SCUBA-2 850 μm map, such that the final map has a pixel size of 4″.

Figure 11 shows the Herschel-derived temperature map of the observed region. The average temperatures are 74 ± 11 and 43 ± 10 K for M17-N and M17-S, respectively. Globally, the dust temperature in M17 gradually decreases from east to west and from north to south. This general trend is consistent with the scenario in which dust is heated by the massive star cluster (see, e.g., Figure 10). The higher temperatures in M17-N and the eastern and northeastern parts of M17-S arise from the fact that these regions are located next to the star cluster and thus strongly heated by this intense radiation source, as well as by the H II region in the east. In M17-S, the dust temperatures

decrease along the direction leading away from the star cluster, which stems from dust absorption within structures with densities an order of magnitude higher than those in M17-N.

5.3. Polarization Fraction versus Emission Intensity, Column Density, and Dust Temperature

We now study the dependence of the polarization fraction, p, on the total intensity, I, the column density, $N(H_2)$, and the dust temperature, T_d. These relationships reveal basic properties of grain alignment and disruption in M17.

First, we investigate the relationship between p and I. It can be clearly seen from Figure 3 that polarization fraction decreases when intensity increases. Generally, the function $p \propto I^{-\alpha}$ describes the variation of the grain alignment efficiency and the magnetic field geometry across the cloud. For a uniform magnetic field, a slope of $\alpha = 1$ implies that the grain alignment is present only in the outer layer of the cloud and becomes completely lost in the inner region (e.g., Pattle et al. 2019). Figure 12 shows a fitted power-law model $p \propto I^{-\alpha}$ with a power-law index $\alpha = 0.51 \pm 0.01$ for the whole M17 region. The values of α do not change much when we fit only pixels from M17-N ($\alpha = 0.54 \pm 0.02$) or M17-S ($\alpha = 0.55 \pm 0.01$) separately. A best-fit value of $\alpha = 0.51$ suggests that
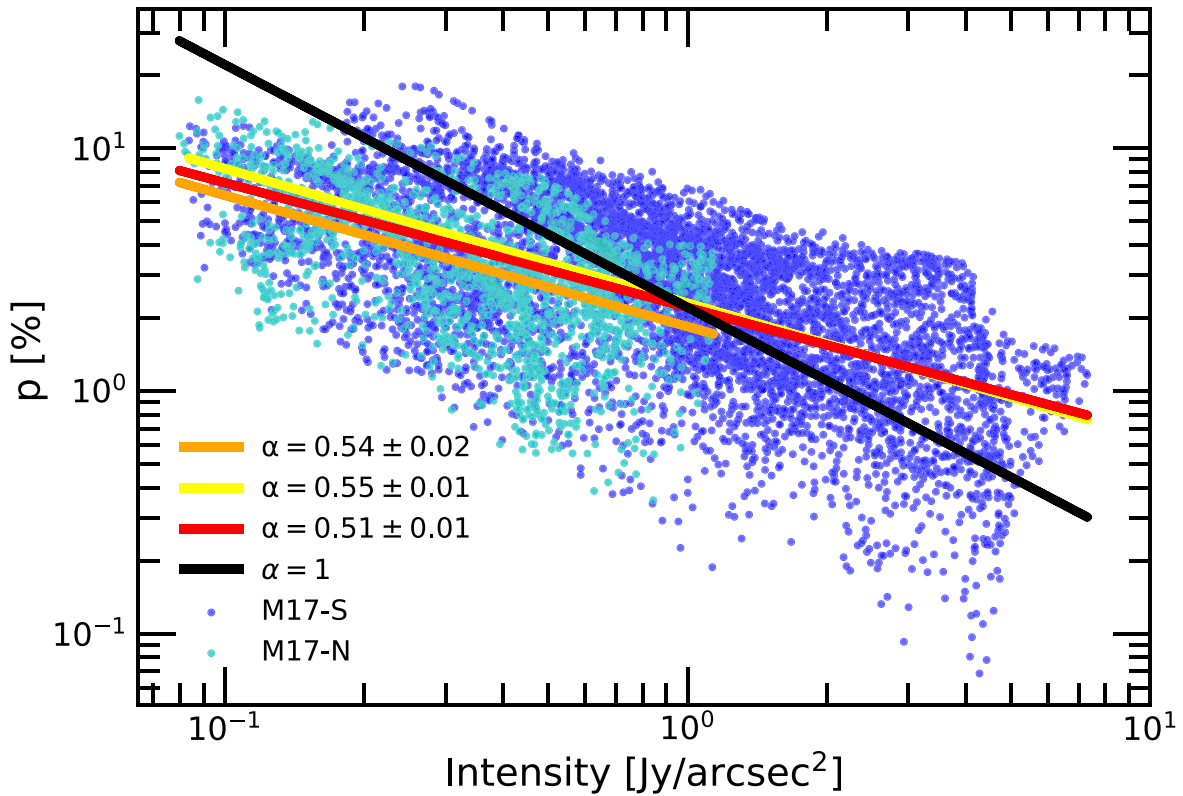
Figure 12. The variation of polarization fraction with total intensity. The orange, yellow, and red lines are the best fits to a power-law model for M17-N, M17-S, and the whole map, respectively. The black solid line is the same power-law model with $\alpha = 1$.

grains remain aligned along sightlines toward regions of high emission intensity (e.g., Pattle et al. 2019).

In order to better understand the variation in p, we now study the relationship between p and $N(H_2)$, as well as between p and T_d. Figure 13 (top left panel) shows the $p - N(H_2)$ relation. Here, we determine the slopes by fitting piecewise linear functions to the data. In the M17-S region, the polarization fraction gradually decreases with increasing gas column density, before it experiences a steep drop, with a slope of -0.71, for $N_{H_2} > 3 \times 10^{22}$ cm^{-2} or visual extinction[15] $A_V > 37$ mag for the typical total-to-selective extinction $R_V \approx 3.1$. In the M17-N region, a steep decrease, with a slope of -0.67, occurs at $N(H_2) > 5 \times 10^{21}$ cm^{-2} or $A_V > 6$ mag. This strong depolarization occurs in the region where the gas density is relatively low and the dust temperature is relatively high compared to that of M17-S (see Figure 11).

The top right panel of Figure 13 shows the $p - T_d$ relation. It appears that the polarization fraction first decreases, then increases, before decreasing again as the dust temperature increases. The decrease-increase feature originates from the M17-S region, while the depolarization arises from from M17-N.

The bottom panel of Figure 13 shows gas column density as a function of dust temperature. The column density decreases rapidly with increasing T_d in M17-S, but varies slowly in M17-N. The first decrease of p for $T_d < 40$ K corresponds to the highest gas density ($A_V \sim 100$ mag). This depolarization is caused by a decrease of grain alignment due to the attenuation of the radiation field and the enhancement of collisional damping. Toward higher dust temperatures, the gas density

drops, and the grain alignment efficiency is enhanced toward the central luminous source, which results in the subsequent increase of p with T_d. These features are expected in the context of the RAT-A theory. However, in M17-N, the dust temperature could be up to 150 K and the gas density becomes more diffuse at $A_V < 10$ mag, while the polarization fraction appears to monotonically decrease as T_d increases, which is completely contradictory to what is expected from RAT-A theory.

5.4. Implications for Grain Alignment and Rotational Disruption by RAT

We now discuss the implications of the observed polarization fraction toward M17 for the physics of grain alignment and disruption based on radiative torques.

According to the RAT-A theory (see Lazarian & Hoang 2007), the polarization fraction of thermal emission increases with decreasing alignment size, a_{align} (the minimum size of aligned grains). The alignment size is determined by the balance between spin-up by RAT and spin-down by gas collisional damping, which is a function of the local dust temperature (or radiation intensity) and gas density, with $a_{align} \sim n_H^{2/7} T_d^{-12/7}$ (Tram et al. 2021). As a result, denser gas and lower dust temperature increase a_{align} (see details in Hoang et al. 2021), which results in a decrease in polarization fraction. This prediction of RAT-A theory can explain the decrease in polarization fraction with increasing gas column density, which we observe in the M17-S region (see Figure 13; left panel). However, it cannot explain the decrease in p with increasing T_d in the M17-N region, where the gas density changes slowly (see Figure 13, right panel). This observation reveals evidence of the RAT-D effect.

---

[15] $A_V(\text{mag}) = R_V \times 2N(H_2)/(5 \times 10^{21} \text{ cm}^{-2})$.
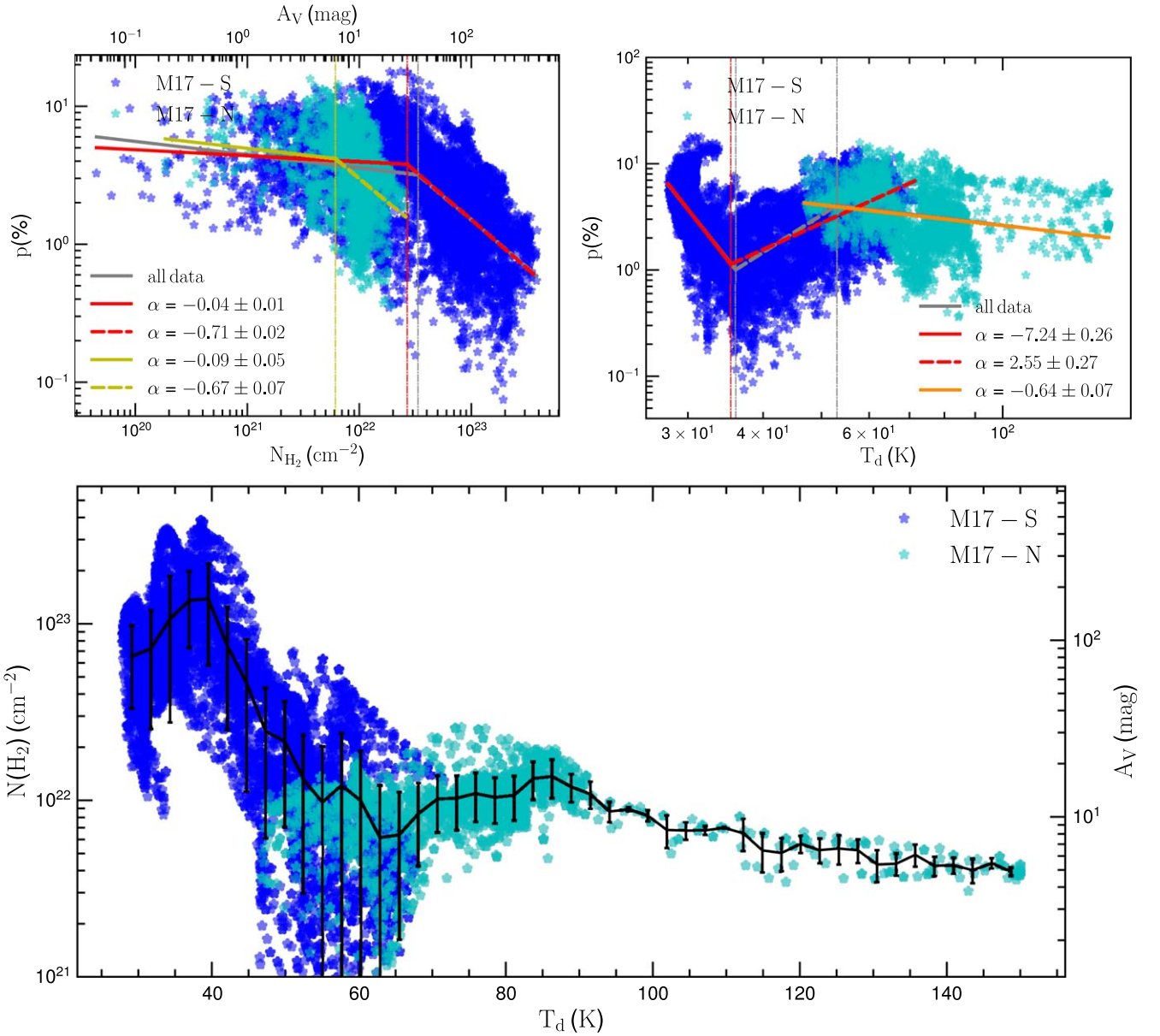
Figure 13. Upper left panel: the relationship between polarization fraction and column density. Upper right: the relationship between polarization fraction and temperature. In both panels, α is the index of the best-fitting power-law model. The SOFIA/HAWC+ polarization map is smoothed to the $14''$ angular resolution of SCUBA-2 at 850 μm, data from which which were used together with Herschel data to get the $N(H_2)$ and T_d maps. Bottom: the variation of the gas column density, $N(H_2)$, with the dust temperature, T_d.

The polarization fraction at far-IR/submillimeter wavelengths is very sensitive to the maximum size of the grain size distribution, because large grains dominate long-wavelength emission. Under the RAT-D mechanism (Hoang et al. 2019), the maximum grain size above which large grains are disrupted by RATs is determined by the local dust temperature (i.e., the radiation field), the gas density, and the grain tensile strength, S_{max}, which result in a grain disruption size $a_{disr} \sim n_H^{1/2} T_d^{-3} S_{max}^{1/4}$ (Tram et al. 2021). For the average estimated volume density $n_{H_2} \simeq 3 \times 10^4$ cm^{-3} (see Table 1), and the temperature at the breaking point in Figure 13 of $T_d \simeq 53$ K, one obtains $a_{disr} = 0.16$, 0.28, and 0.49 μm for radiation energy densities of $S_{max} = 10^7$, 10^8, and 10^9 erg cm^{-3}, assuming a mean wavelength of the radiation field of 1 μm. The decrease in the disruption size with increasing T_d predicted by RAT-D leads to a decrease in the dust polarization

fraction as T_d increases (Lee et al. 2020; Tram et al. 2021b), which successfully reproduces the trend that we observe in M17-N (see Figure 13).

To quantify the effect of magnetic field tangling at small scales on the depolarization that we observe, we calculate the polarization angle dispersion function, S, (see Section 3.3 in Planck Collaboration et al. 2015). For a pixel at location x, S is calculated as the standard deviation of the polarization angle difference, S_{xi}, between pixel x and pixel i which lies on a circle having x as the center and a radius of δ, such that

$$S^2(x, \delta) = \frac{1}{N}\sum_{i=1}^{N} S_{xi}^2, \qquad (19)$$

where $S_{xi} = \theta(x) - \theta(x + \delta)$ is the polarization angle difference and N is the number of pixels lying on the circle.
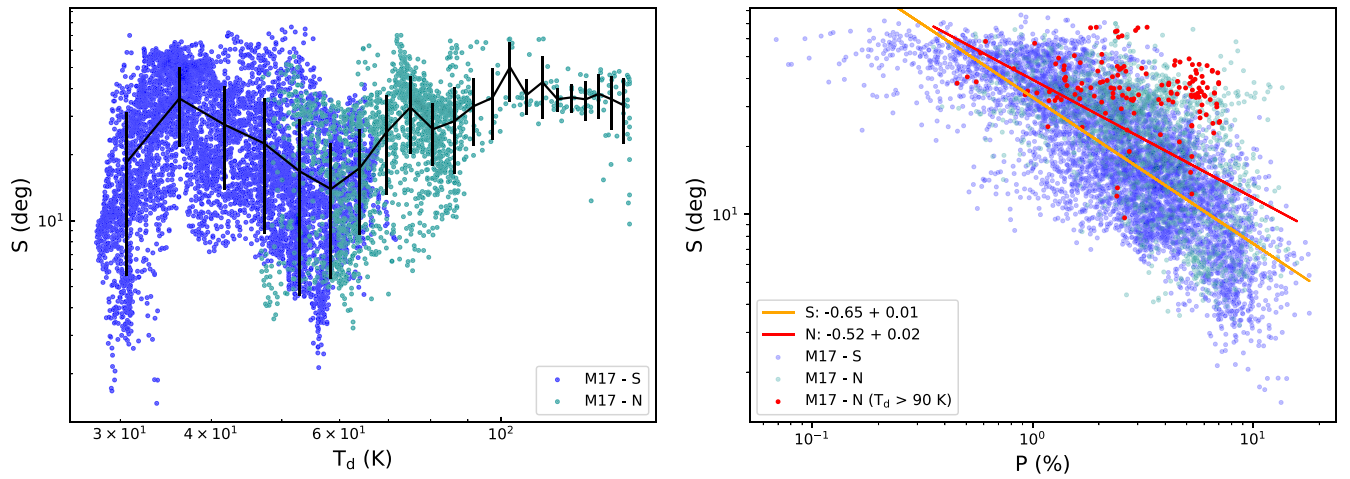
Figure 14. Left: variation of the polarization angle dispersion function, S, with the dust temperature, T_d. The black curve shows the mean and the standard deviation per bin. Right: variation of S with the polarization fraction, p. Red dots are pixels with $T_d > 90$ K. The orange and red lines are fits to a power-law model for M17-N and M17-S, respectively.

For our SOFIA/HAWC+ data set, we calculate S for $\delta = 27\rlap{.}''2$ ($\sim$2 beam sizes). The left panel of Figure 14 shows the S–T_d relation, in which it can be seen that the angular dispersion function S is strongly correlated with dust temperature, except at the highest values, $T_d > 90$ K, in M17-N. Thus, the decline of p at $T_d > 90$ K (see the upper right panel of Figure 13) cannot be explained by magnetic field tangling and so provides evidence for the RAT-D effect. The right panel of Figure 14 shows a general anticorrelation between S and p except, again, for the highest-temperature pixels (red dots), whose temperatures are greater than 90 K. For pixels with $T_d < 35$ K located in M17-S (dark blue dots in Figures 13 and 14), we can see that the rapid decrease in p is due to B-field tangling in the high-density region (see bottom panel of Figure 13). In the 35–65 K temperature range, in both M17-N and M17-S, both $N(H_2)$ and S decrease, and therefore, p increases. This clearly shows the important contribution of field tangling to depolarization at low dust temperatures.

Detailed modeling of dust polarization in M17 using models of grain alignment and disruption by RATs is beyond the scope of this paper, and will be addressed in a follow-up study.

6. Summary

In this study, we use SOFIA/HAWC+ dust polarization observations at 154 μm to study magnetic fields and dust physics in the M17 nebula. Our main results are summarized as follows:

1. Using the DCF method, we estimated the magnetic field strengths to be 980 ± 230 μG in the lower-density region (M17-N) and 1665 ± 885 μG in the higher-density region (M17-S). This strong magnetic field could be a result of pressure exerted by the H II region in the eastern part of the region of M17 observed by SOFIA/HAWC+. In M17-N, the B-field morphology may be that of a gravitationally collapsing molecular core. The B-field morphology in M17-S is well-organized, and elongated along the direction of gravitational collapse from the outer regions to the denser central regions. The fields are dragged inward toward the center of gravity. The B-field morphology represents an asymmetric large-scale hourglass structure. We also found a pillar structure, which is

one of the common features of PDR regions. A rough estimate of the relative contributions of ram and magnetic pressures suggests that the wind from the PDR region is strong enough to impact on the B-field morphology of M17.

2. The Alfvénic Mach numbers are determined to be sub-Alfvénic ($\mathcal{M}_A < 1$), which indicate that the magnetic field dominates over turbulence. In addition, the sub-critical mass-to-flux ratio values which we infer, $\lambda < 1$, imply that the magnetic fields in the regions are strong enough to resist gravitational collapse. These results are consistent with the deficiency in the formation of massive stars in the region found by previous studies.

3. There are large statistical biases on the estimation of the polarization angle dispersion, σ_θ, as well as on the volume density, $n(H_2)$, due to the fact that the magnetic field strengths are estimated over large areas. These biases lead to large uncertainties on the measurements of the magnetic field strength. It is also known that for a random sample of magnetic field orientations, using the DCF method the mass-to-flux ratio will on average be overestimated by a factor $\sim$3 due to geometric effects. Conversely, using the method proposed by Cho & Yoo (2016) to account for LOS integration effects, we found the magnetic field strength to have been overestimated by factors of 1.1 and 3.9 for M17-N and M17-S, respectively. Therefore, new methods of estimating magnetic field strength which are able to accurately measure the field strength and accompanying useful parameters such as Alfvénic Mach numbers and mass-to-flux ratios on a pixel-by-pixel basis would provide more precise and detailed information on the conditions for star formation in the M17 MC.

4. To study dust physics, we analyzed the relationship between the polarization fraction, p, and the emission intensity, I, gas column density, $N(H2)$, and dust temperature, T_d. The power index of the p versus I relation, $\alpha = 0.51$, implies that dust grains could still be aligned by radiation in the region. The decrease of dust polarization with column density in M17-S can be explained by the RAT-A theory as well as by tangling of the magnetic field.

5. To study the effect of magnetic field tangling on the dust polarization, we also analyzed the variation of the polarization angle dispersion function, S, with dust temperature and gas column density. In M17-N, the decrease of p with T_d at high temperatures when both $N(H_2)$ and S decrease is most consistent with the theoretical predictions for dust polarization resulting from both the RAT-A and RAT-D effects.

Appendix

This appendix shows the characteristics of the observational data and the behavior of the master cut applied to the data.

Figure A1 shows the distributions of the S/Ns of I, p, and I_p before and after applying the master cut defined in the text. Their corresponding mean and rms values are listed in Table A1. The mean values of the S/Ns increase significantly after the cut, by 45%, 18%, and 17% for I, p, and I_p, respectively.

Figure A2 presents one-dimensional histograms of the raw data of I, σ_I, p, σ_p, I_p, σ_{I_p}, θ, and σ_θ. The associated mean and rms values of these quantities are presented in Table A2.

Figure A3 defines the upper and lower regions used for the data analysis. We present the two sub-figures with different total intensity scales, in order to better visualize the emission structure of the two regions.

Figure A4 presents the highest-density region of M17-S, with a cut on $N(H_2) > 10^{22}\,\mathrm{cm}^{-2}$ applied.

Table A1
Means and rms Values of the Distributions of S/N_I, S/N_p, S/N_{I_p}

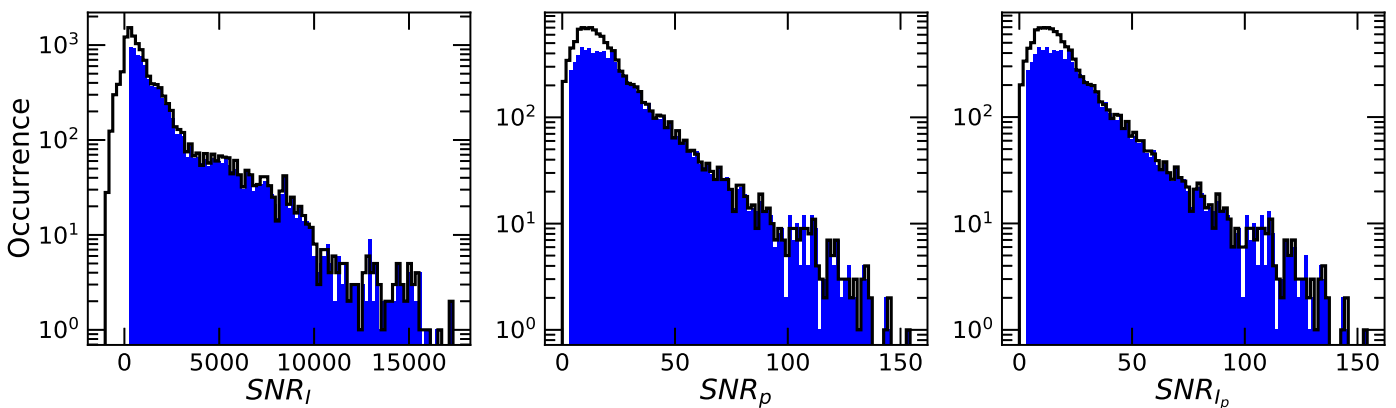|		S/N_I	S/N_p	S/N_{I_p}
Before cut	Mean	1477.4	22.2	22.3
	rms	2186.3	19.6	19.6
After cut	Mean	2138.5	26.1	26.1
	rms	2366.7	20.8	20.9

Figure A1. Left to right: distributions of S/Ns of the total intensity (S/N_I), polarization fraction (S/N_p), and polarization intensity (S/N_{I_p}). The unfilled histograms show the distribution before the cut is applied, while the blue histograms show the distribution after the cut.
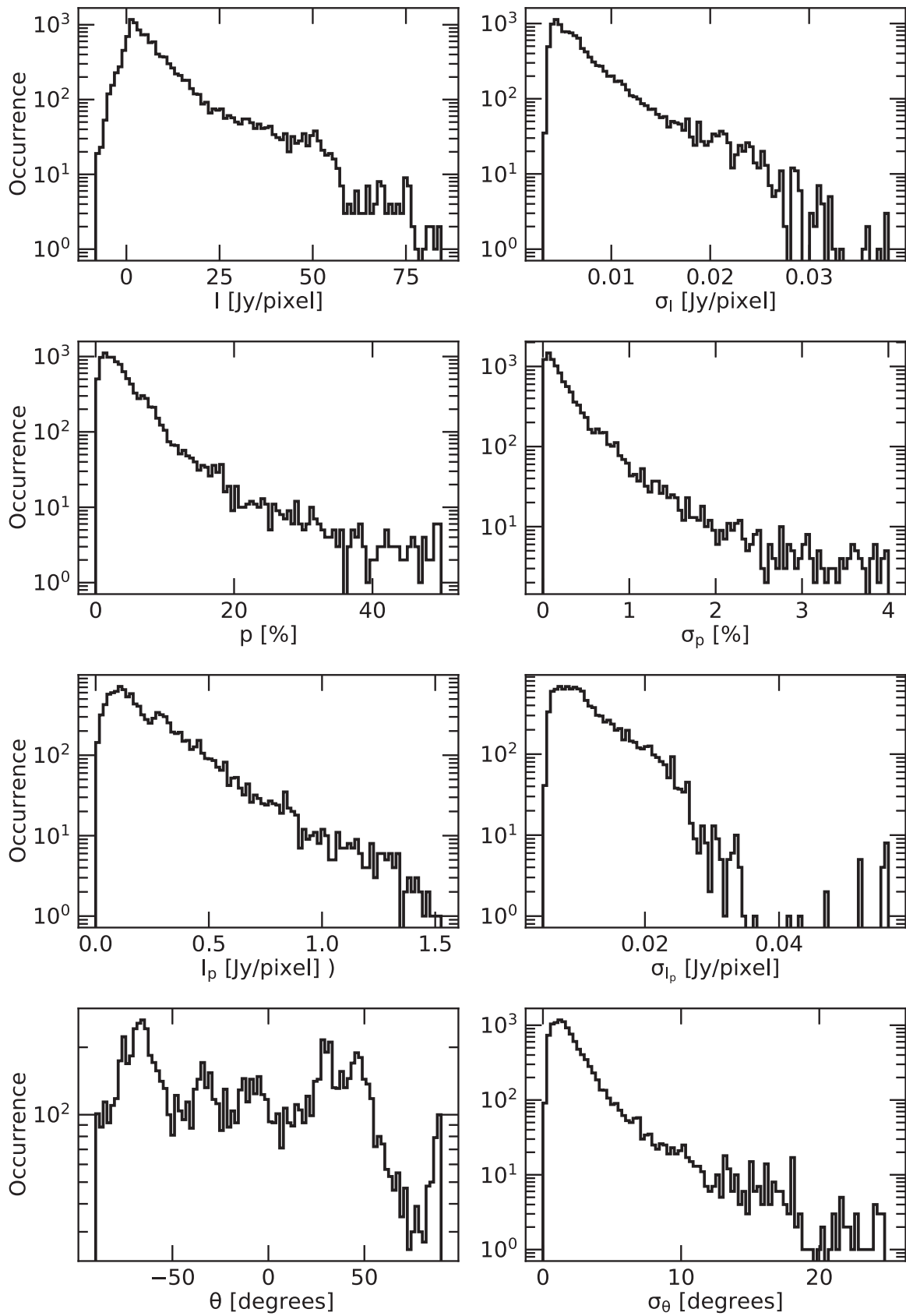
Figure A2. From left to right, top to bottom: distributions of I, σ_I, p, σ_p, I_p, σ_{I_p}, θ, and σ_θ for the raw SOFIA/HAWC+ data.
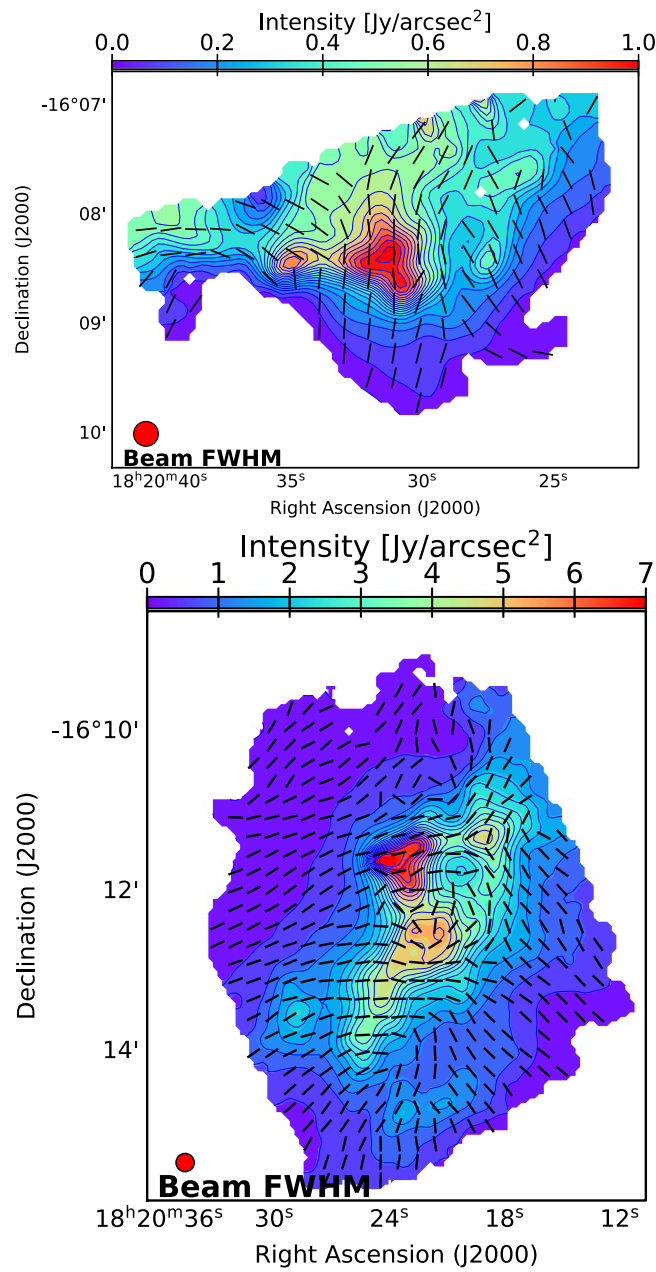
Figure A3. A close-up view of B-fields in the SOFIA/HAWC+ M17 regions: M17-N (top) and M17-S (bottom). Description of the maps is the same as that for Figure 3.

Table A2
Mean and rms Values of I, σ_I, I_p, σ_{I_p}, p, σ_p, θ, and σ_θ

	I [Jy pixel^{-1}]	σ_I [Jy pixel^{-1}]	I_p [Jy pixel^{-1}]	σ_{I_p} [Jy pixel^{-1}]	p [%]	σ_p [%]	θ [°]	σ_θ [°]
Mean	9.4	0.0078	0.247	0.0119	5.0	0.367	−11.1	2.5
rms	12.7	0.0046	0.215	0.0054	5.9	0.507	48.9	2.8

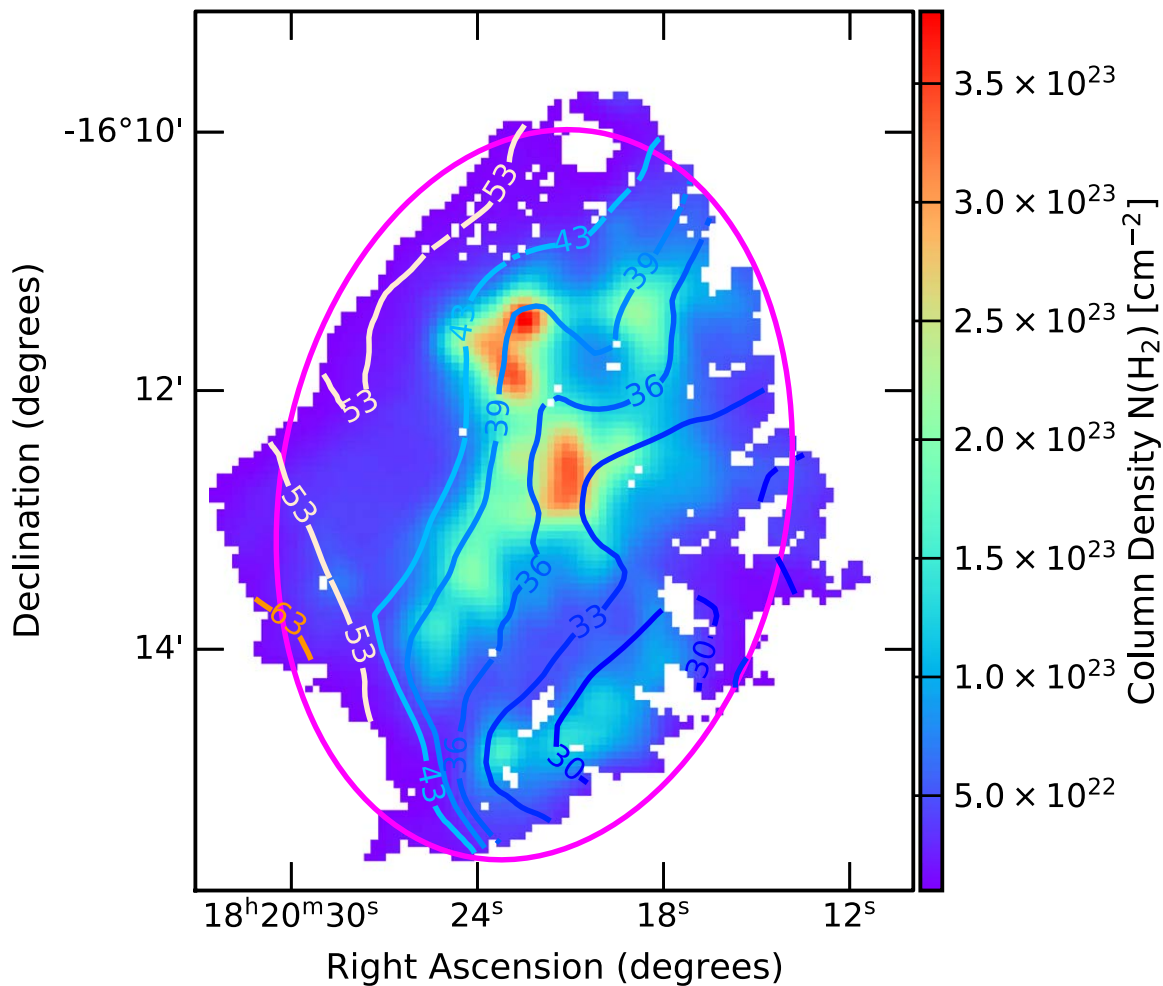**Figure A4.** The highest-density region of M17-S, with $N(H_2) > 10^{22}$ cm^{-2}. The ellipse is centered at R.A. $\sim 18^h20^m22\overset{s}{.}17$, decl. $\sim -16°12'48''.3$, with major $\times$ minor axes of $171'' \times 118''$, and a position angle of $350°$. The contours represent the dust temperature.

ORCID iDs

Thuong Duc Hoang ⓘ https://orcid.org/0000-0002-3437-5228
Nguyen Bich Ngoc ⓘ https://orcid.org/0000-0002-5913-5554
Pham Ngoc Diep ⓘ https://orcid.org/0000-0002-2808-0888
Le Ngoc Tram ⓘ https://orcid.org/0000-0002-6488-8227
Thiem Hoang ⓘ https://orcid.org/0000-0003-2017-0982
Kate Pattle ⓘ https://orcid.org/0000-0002-8557-3582
Wanggi Lim ⓘ https://orcid.org/0000-0003-4243-6809
Ngan Le ⓘ https://orcid.org/0000-0003-1990-1717
Dieu D. Nguyen ⓘ https://orcid.org/0000-0002-5678-1008
Nguyen Fuda ⓘ https://orcid.org/0000-0002-6372-8395
Gia Bao Truong Le ⓘ https://orcid.org/0000-0001-9654-8051
Hien Phan ⓘ https://orcid.org/0000-0003-4935-462X
Nguyen Chau Giang ⓘ https://orcid.org/0000-0002-3681-671X

References

Andersson, B.-G., Lazarian, A., & Vaillancourt, J. E. 2015, ARA&A, 53, 501
Astropy Collaboration, Price-Whelan, A. M., SipHocz, B. M., et al. 2018, AJ, 156, 123
Astropy Collaboration, Robitaille, T. P., Tollerud, E. J., et al. 2013, A&A, 558, A33
Beuther, H., Soler, J. D., Linz, H., et al. 2020, ApJ, 904, 168
Brogan, C. L., Troland, T. H., Roberts, D. A., & Crutcher, R. M. 1999, ApJ, 515, 304
Cabral, B., & Leedom, L. C. 1993, in Proc. 20th Annual Conf. on Computer Graphics and Interactive Techniques, SIGGRAPH '93, ed. J. T. Kajiya (New York: ACM), 263
Chandrasekhar, S., & Fermi, E. 1953, ApJ, 118, 113
Chen, Z., Jiang, Z., Wang, Y., et al. 2012, PASJ, 64, 110
Cho, J., & Yoo, H. 2016, ApJ, 821, 21
Chuss, D. T., Andersson, B.-G., Bally, J., et al. 2019, ApJ, 872, 187
Crutcher, R. M. 2004, in The Magnetized Interstellar Medium, ed. B. Uyaniker, W. Reich, & R. Wielebinski (Katlenburg-Lindau: Copernicus), 123
Crutcher, R. M. 2012, ARA&A, 50, 29
Davis, L. 1951, PhRv, 81, 890
Dolginov, A. Z., & Mytrophanov, I. G. 1976, Ap&SS, 43, 291
Dotson, J. L. 1996, ApJ, 470, 566
Draine, B. T., & Weingartner, J. C. 1996, ApJ, 470, 551
Draine, B. T., & Weingartner, J. C. 1997, ApJ, 480, 633
Elmegreen, B. G. 2000, ApJ, 530, 277
Falceta-Gonçalves, D., Lazarian, A., & Kowal, G. 2008, ApJ, 679, 537
Federrath, C. 2016, JPhCS, 719, 012002
Ginsburg, A., Koch, E., Robitaille, T., et al. 2019, radio-astro-tools/spectral-cube: v0.4.4, Zenodo, doi:10.5281/zenodo.2573901
Gordon, M. S., Lopez-Rodriguez, E., Andersson, B. G., et al. 2018, arXiv:1811.03100
Hanson, M., Howarth, I., & Conti, P. 1997, ApJ, 489, 698
Harper, D. A., Runyan, M. C., Dowell, C. D., et al. 2018, JAI, 07, 1840008
Hennebelle, P., & Inutsuka, S.-i. 2019, FrASS, 6, 5
Hildebrand, R. H., Kirby, L., Dotson, J. L., Houde, M., & Vaillancourt, J. E. 2009, ApJ, 696, 567
Hoang, T. 2020, Galax, 8, 52
Hoang, T., & Lazarian, A. 2009, ApJ, 697, 1316
Hoang, T., & Lazarian, A. 2016, ApJ, 831, 159

Hoang, T., Tram, L. N., Lee, H., & Ahn, S.-H. 2019, NatAs, 3, 766
Hoang, T., Tram, L. N., Lee, H., Diep, P. N., & Ngoc, N. B. 2021, ApJ, 908, 218
Houde, M., Bastien, P., Dotson, J. L., et al. 2002, ApJ, 569, 803
Kandori, R., Tomisaka, K., Tamura, M., et al. 2018, ApJ, 865, 121
Kleinmann, D. E., & Wright, E. L. 1973, ApJL, 185, L131
Lazarian, A., Andersson, B.-G., & Hoang, T. 2015, in Polarimetry of Stars and Planetary Systems, ed. L. Kolokolova, J. Hough, & A.-C. Levasseur-Regourd (Cambridge: Cambridge Univ. Press), 81
Kritsuk, A. G., Ustyugov, S. D., & Norman, M. L. 2017, NJPh, 19, 065003
Lazarian, A., & Hoang, T. 2007, MNRAS, 378, 910
Lee, H., Hoang, T., Le, N., & Cho, J. 2020, ApJ, 896, 44
Lee, K., Looney, L., Johnstone, D., & Tobin, J. 2012, ApJ, 761, 171
Li, D. L., Esimbek, J., Zhou, J.-J., et al. 2014, A&A, 567, A10
Li, P. S., & Klein, R. I. 2019, MNRAS, 485, 4509
Lim, W., Buizer, J. M. D., & Radomski, J. T. 2020, ApJ, 888, 98
Lim, W., Tan, J. C., Kainulainen, J., Ma, B., & Butler, M. J. 2016, ApJ, 829, L19
Liu, J., Zhang, Q., Commercon, B., et al. 2021, ApJ, 919, 79
Liu, J., Zhang, Q., Qiu, K., et al. 2020, ApJ, 895, 142
Mac Low, M.-M., & Klessen, R. S. 2004, RvMP, 76, 125
McKee, C. F., & Ostriker, E. C. 2007, ARA&A, 45, 565
Nakamura, F., Ishii, S., Dobashi, K., et al. 2019, PASJ, 71, 5
Nakamura, F., & Li, Z.-Y. 2008, ApJ, 687, 354
Nakano, T., & Nakamura, T. 1978, PASJ, 30, 671
Ngoc, N. B., Diep, P. N., Parsons, H., et al. 2021, ApJ, 908, 10
Ostriker, E. C., Stone, J. M., & Gammie, C. F. 2001, ApJ, 546, 980
Padoan, P., Goodman, A., Draine, B. T., et al. 2001, ApJ, 559, 1005
Padoan, P., & Nordlund, A. 1999, ApJ, 526, 279
Pattle, K., & Fissel, L. 2019, FrASS, 6, 15
Pattle, K., Lai, S.-P., Hasegawa, T., et al. 2019, ApJ, 880, 27
Pattle, K., Ward-Thompson, D., Berry, D., et al. 2017, ApJ, 846, 122
Pattle, K., Ward-Thompson, D., Hasegawa, T., et al. 2018, ApJ, 860, L6
Pellegrini, E. W., Baldwin, J. A., Brogan, C. L., et al. 2007, ApJ, 658, 1119
Planck Collaboration, Ade, P. A. R., Aghanim, N., et al. 2015, A&A, 576, A104
Pomohaci, R., Oudmaijer, R. D., Lumsden, S. L., Hoare, M. G., & Mendigutía, I. 2017, MNRAS, 472, 3624
Povich, M. S., Churchwell, E., Bieging, J. H., et al. 2009, ApJ, 696, 1278
Reid, M. A., & Wilson, C. D. 2006, ApJ, 644, 990
Robitaille, T. 2019, APLpy v2.0: The Astronomical Plotting Library in Python, Zenodo, doi:10.5281/zenodo.2567476
Robitaille, T., Deil, C., & Ginsburg, A. 2020, Reproject: Python-based astronomical image reprojection, Astrophysics Source Code Library, ascl:2011.023
Sanhueza, P., Girart, J. M., Padovani, M., et al. 2021, ApJ, 915, L10
Seifried, D., & Walch, S. 2015, MNRAS, 452, 2410
Serkowski, K. 1962, AdA&A, 1, 289
Sugitani, K., Nakamura, F., Shimoikura, T., et al. 2019, PASJ, 71, S7
Temi, P., Hoffman, D., Ennico, K., & Le, J. 2018, JAI, 07, 1840011
Tram, L. N., Hoang, T., Lee, H., et al. 2021a, ApJ, 906, 115
Tram, L. N., Hoang, T., Lopez-Rodriguez, E., et al. 2021, ApJ, 923, 130
Tram, L. N., Lee, H., Hoang, T., et al. 2021b, ApJ, 908, 159
Wang, J.-W., Lai, S.-P., Eswaraiah, C., et al. 2019, ApJ, 876, 42
Ward-Thompson, F., McKee, T., Furuya, R., & Tsukamoto, Y. 2020, FrASS, 7, 13
Wardle, J. F. C., & Kronberg, P. P. 1974, ApJ, 194, 249
Wurster, J., & Li, Z.-Y. 2018, FrASS, 5, 39
Xu, Y., Moscadelli, L., Reid, M. J., et al. 2011, ApJ, 733, 25
Zeng, L., Bennett, C. L., Chapman, N. L., et al. 2013, ApJ, 773, 29